

The star formation history and metal content of the “Green Peas”. New detailed GTC-OSIRIS spectrophotometry of three galaxies

R. Amorín¹, E. Pérez-Montero and J.M. Vílchez

Instituto de Astrofísica de Andalucía-CSIC, Glorieta de la Astronomía S/N, E-18008 Granada, Spain
and

P. Papaderos

Centro de Astrofísica and Faculdade de Ciências, Universidade do Porto, Rua das Estrelas, 4150-762 Porto, Portugal

ABSTRACT

We present deep broad-band imaging and long-slit spectroscopy of three compact, low-mass starburst galaxies at redshift $z \sim 0.2\text{--}0.3$, also referred to as Green Peas (GP). We measure physical properties of the ionized gas and derive abundances for several species with high precision. We find that the three GPs display relatively low extinction, low oxygen abundances, and remarkably high N/O ratios. We also report on the detection of clear signatures of Wolf-Rayet (WR) stars in these galaxies. We carry out a pilot spectral synthesis study using a combination of both population and evolutionary synthesis models. Their outputs are in qualitative agreement, strongly suggesting a formation history dominated by starbursts. In agreement with the presence of WR stars, these models show that these GPs currently undergo a major starburst producing between $\sim 4\%$ and $\sim 20\%$ of their stellar mass. However, as models imply, they are old galaxies having had formed most of their stellar mass several Gyr ago. The presence of old stars has been spectroscopically verified in one of the galaxies by the detection of Mg I $\lambda\lambda 5167, 5173$ absorption line. Additionally, we perform a surface photometry study based on HST data, that indicates that the three galaxies possess an exponential low-surface brightness envelope. If due to stellar emission, the latter is structurally compatible to the evolved hosts of luminous BCD/HII galaxies, suggesting that GPs are identifiable with major episodes in the assembly history of local BCDs. These conclusions highlight the importance of these objects as laboratories for studying galaxy evolution at late cosmic epochs.

Subject headings: galaxies: abundances — galaxies: dwarf — galaxies: evolution — galaxies: starburst

1. INTRODUCTION

“Green Peas” (GPs) are convenient laboratories to study galaxy assembly at relatively low redshifts ($0.11 \lesssim z \lesssim 0.35$). These compact, high-surface brightness systems were recently identified on images from the Sloan Digital Sky Sur-

vey (SDSS) Data Release 7 by volunteers in the “Galaxy Zoo” project (Lintott et al. 2008, 2011). Their nickname reflects their point-like appearance and “green” color on SDSS image overlays. The latter is a consequence of very strong [O III] $\lambda 5007$ line emission, with equivalent widths of up to ~ 2000 Å, enhancing the observed SDSS r fluxes at those redshifts. Such an extreme nebular emission contribution has so far been documented in extremely metal-poor blue compact

¹CONSOLIDER-GTC fellow;
Email: amorin@iaa.es

dwarf galaxies (XBCDs) only (Terlevich et al. 1991; Izotov et al. 1997; Papaderos et al. 1998, 2008) in addition to a few ultra-compact star-bursting dwarfs in galaxy clusters (Reverte et al. 2007).

The GPs were first studied in detail by Cardamone et al. (2009) (hereafter C09), who showed that these galaxies reside in lower-density environments and are very rare (~ 2 galaxies deg^{-2} brighter than 20.5 mag). A subset of 80 GPs with decent signal-to-noise (S/N) SDSS spectra was spectroscopically characterized as purely star-burst systems. On average, these galaxies appear luminous in both optical ($M_B \sim -20$ mag) and UV ($L_{FUV} \sim 3 \times 10^{10} L_\odot$) wavelengths, and are characterized by high surface brightness and very compact appearance (typical sizes $\lesssim 5$ kpc). According to C09, the GPs are low-mass galaxies (stellar masses $M_\star < 10^{10.5} M_\odot$) with prodigious star formation rates (SFR up to $60 M_\odot \text{ yr}^{-1}$) and low intrinsic reddening ($E(B-V) \lesssim 0.25$). In particular, their specific star formation rates (sSFR in the range 10^{-7} to 10^{-9} yr^{-1}) are among the highest inferred in the nearby Universe (cf e.g., Brinchmann et al. 2004; Salim et al. 2007), and well in the range of those of high-redshift galaxies (e.g., Bauer et al. 2005).

Chemical abundances of the ionized gas have provided important additional clues about the nature of the GPs. Oxygen abundance determinations, based on the direct (T_e) method led Amorín et al. (2010) (hereafter A10) to conclude that the GPs in the Cardamone’s sample are genuinely metal-poor galaxies, spanning a range of values $7.6 \lesssim 12+\log(\text{O}/\text{H}) \lesssim 8.4$ with an average of one fifth of the solar value in their gas-phase metallicity in their gas-phase metallicity. Their results were recently confirmed by Izotov et al. (2011) (hereafter Iz11), who pointed out that GPs are a subset of luminous compact galaxies showing chemical abundances similar to lower-luminosity Blue Compact Dwarfs (BCDs).

Interestingly, the position of the GPs in the fundamental relation between stellar mass and metallicity (the mass-metallicity relation, MZR), and between B -band luminosity and metallicity (the luminosity-metallicity relation, LZR) appear systematically offset (up to ~ 0.3 dex in the MZR) to lower abundances when compared with the bulk of local star-forming galaxies (SFGs) from the SDSS

(A10, Iz11, see also Amorín et al. 2011). Their location in the MZR, and also in the LZR, appear to form a distinct sequence, along with nearby XBCDs (I Zw 18 or SBS 0335-052, Guseva et al. 2009) and some luminous BCDs at low (Bergvall & Östlin 2002, Iz11) and intermediate redshifts (e.g., Hoyos et al. 2005; Kakazu et al. 2007; Salzer et al. 2009) and most SFGs at high redshift (e.g., Pettini et al. 2001; Erb et al. 2006; Pérez-Montero et al. 2009; van der Wel et al. 2011; Finkelstein et al. 2011).

In this context, ionic abundance ratios between species with an assumed different stellar origin are important to probe the chemical evolution of the GPs. This is the case of the nitrogen-to-oxygen ratio (N/O), since the nitrogen and oxygen yields are driven by stars of different mass, therefore it gives relevant information about the SF rate and history of SFGs (e.g. Mollá et al. 2006). In metal-poor SFGs ($12+\log(\text{O}/\text{H}) \lesssim 8$), nitrogen production is expected to have mainly a primary origin, owing to massive stars. Then, in the O/H vs. N/O diagram, they form a *plateau* at $\log(\text{N}/\text{O}) \sim -1.5$ (Alloin et al. 1979; Campbell et al. 1986; Izotov & Thuan 1999; Pilyugin et al. 2003), with a relatively large vertical dispersion (e.g., Garnett 1990; Pilyugin 1993; Henry et al. 2006; Nava et al. 2006; van Zee & Haynes 2006; Pérez-Montero & Contini 2009). For example, BCDs in the range $12+\log(\text{O}/\text{H}) \sim 7.6-8.2$, generally show low N/O ratios between -1.54 and -1.27 (Nava et al. 2006), with few exceptions only (see also Fig. 1 in Henry et al. (2006)). By contrast, the nitrogen production in metal-rich SFGs ($12+\log(\text{O}/\text{H}) > 8.2$) has mainly a secondary origin, powered by low- to intermediate-mass stars, which produce a positive correlation between N/O and O/H (e.g., Vila Costas & Edmunds 1993). Intriguingly enough, *GPs show systematically larger N/O ratios compared to most SFGs at the same oxygen abundance* (A10, see also Amorín et al. 2011; Pilyugin et al. 2012), being in most cases located above the *plateau*. Their N/O ratios, however, seem to be normal for SFGs of similar stellar masses.

The known global properties of the GPs support the view that these galaxies go through a short and extreme phase in their evolution. However, in order to confirm this and elaborate a coherent evolutionary picture for GPs, important

pieces of the puzzle need to be supplied and investigated. One example is the star formation history (SFH) of GPs, which still is not well-constrained, to a large extent because quantitative studies on the photometric structure and mass contribution of an underlying older stellar host are lacking. In order to establish a physical and evolutionary connection between GPs and nearby BCDs, it is crucial to verify that the structural properties of the host galaxy in both SFG classes are compatible. Whereas such a structural similarity has been demonstrated for luminous compact blue galaxies (LCBGs) at $z \sim 1$ by Noeske et al. (2006), no surface photometry studies for the lower- z GPs exist as yet. Another example is the interpretation of the relations between oxygen and nitrogen abundances, and with stellar mass and SFRs. They were discussed by A10 in terms of the balance between inflows of metal-poor gas (e.g., Köppen & Hensler 2005) and the presence of enriched outflows (e.g., van Zee et al. 1998). However, other scenarios usually invoked to explain large N/O ratios in nearby metal-poor SFGs, such as possible pollution by Wolf-Rayet (WR) stars (e.g., van Zee et al. 1998; Brinchmann et al. 2008; Monreal-Ibero et al. 2010; Berg et al. 2011) were not addressed.

The main reason why the above questions remain open is that, until now, GPs have been mainly studied using SDSS data. This has allowed to infer relevant global properties for a large number of galaxies. The downside, however, is that SDSS spectrophotometric studies are limited by the often poor signal-to-noise (S/N) and sensitivity of the data. These limitations prevent, for example, studies of faint spectral features, like those due to young WR stars or of weak stellar absorption features owing to an old underlying component. Moreover, the moderate to poor S/N of SDSS spectra impacts accurate chemical studies requiring precise measurements of, e.g., the [O III] $\lambda 4363\text{\AA}$ or [N II] $\lambda 6584\text{\AA}$ line fluxes (e.g., A10) as well as stellar mass determinations based on a refined modeling of the spectral energy distribution (SED) of the stellar and gaseous continuum (Iz11).

In this study, we aim at going one step further in the understanding of the properties of GPs by using deep imaging and spectroscopy with the 10.4m Gran Telescopio Canarias (GTC), in addition to archival HST images. These high-quality

data allow us to analyze in better detail the chemical and structural properties of a small sample of GPs. In particular, deep spectra with the GTC are used both to improve on chemical abundance determinations and to study the SFH of GPs using population and evolutionary spectral synthesis models. Faint features, e.g., absorption lines from old stellar populations or signatures of massive and young WR stars, are examined. The latter will provide strong constraints on the age of the young starburst and on the amount of metal pollution in the interstellar medium that can be expected from them as well (e.g., Schaerer & Vacca 1998; Guseva et al. 2000; Brinchmann et al. 2008; Pérez-Montero et al. 2011).

The paper is organized as follows: Section 2 describes the target selection, the GTC-OSIRIS observations and the data reduction, and the HST data. In Section 3 we show the methodology and present the results, which are then discussed in Section 4. Finally, conclusions are given in Section 5. We assume a standard cosmology with $H_0 = 70$, $\Omega_\Lambda = 0.7$, and $\Omega_m = 0.3$.

2. DATA

2.1. Target selection

For the present study we have selected three GPs, SDSS J004054.32+153409.6, SDSS J113303.79+651341.3, and SDSS J232539.22+004507.2 (for simplicity hereafter GP004054, GP113303, and GP232539 respectively) from C09. The main properties of the galaxies as derived from the literature are summarized in Table 1. The three galaxies are at very similar redshifts $z \sim 0.24 - 0.28$ and they are located in relatively isolated regions, with no nearby *bright* companions. These GPs have a high UV surface brightness and luminosity ($\sim 10^{10.5} L_\odot$), translating into large SFRs ($\geq 10 M_\odot \text{ yr}^{-1}$) per unit area. For this reason, they were also included in the sample of ~ 30 super compact, UV luminous galaxies by Hoopes et al. (2007), also known in subsequent studies as local “Lyman-break Analogs” (LBAs Basu-Zych et al. 2007; Overzier et al. 2008, 2009, 2010; Gonçalves et al. 2010). They were, therefore, better studied than other GPs. For example, these galaxies are the three out of four GPs for which spatially resolved HST imaging is publicly available up to date. From HST WFPC2 and ACS imaging (Overzier

et al. 2009) we know that they share similar morphologies, with UV and optical light dominated by few very luminous star-forming clumps superimposed on a compact stellar host (optical half-light radius of about 1 kpc).

2.2. Data set

Deep broad-band imaging and long-slit spectroscopy for the three target galaxies were carried out using the OSIRIS instrument, mounted on the 10.4 m GTC at the Observatorio Roque de los Muchachos (La Palma, Spain).

OSIRIS¹ (Cepa et al. 2000) is an imager and spectrograph for the optical wavelength range (from ~ 3650 to 10000\AA), located in the Nasmyth-B focus of GTC. It consists of two 2048×4096 Marconi CCD42-82 with a 9.2 arcsec gap between them. The unvignetted instrument field of view is 7.8×7.8 arcmin with a pixel scale of 0.125 arcsec. Both imaging and spectroscopic observations were obtained in service mode by the GTC staff during the first semester of 2010. The log of observations is summarized in Table 2.

2.2.1. GTC and HST Imaging

Broad-band imaging for the three targets were obtained using the SDSS z' filter (centered at 9695\AA) in the standard mode (2×2 binning), given a pixel scale of 0.25 arcsec. In order to avoid substantial contamination from strong emission lines and reach faint surface brightness levels, we chose the z' filter despite its efficiency is lower than the i' filter. For each of the three galaxies our broad-band images were taken under different sky transparency conditions. Unfortunately, only GP113303 was observed in a dark night under photometric conditions. The seeing was in all the cases below 1.2 arcsec. Total exposure times of 2250 sec were achieved taking several series of five short exposures (90 sec) in a cross-shape dithering pattern with offsets of 10 arcsec. Series of bias, twilight sky flats, and several spectrophotometric standards were observed during the same nights (see 2.2.3).

The main goal of deep imagery with the GTC was the investigation of the close environment of

our sample GPs e.g., extended tidal low-surface brightness features that could have gone undetected on the shallower SDSS and archival HST images. In Figure 1 we present deep z' -band images for the three GPs. The right gray scale bar and contours in these images show the z' -band surface brightness of the galaxies. Only GP232539 appears to show a somewhat extended (size $>$ FWHM) LSB component. Possible small companions, barely seen on SDSS images, are projected few arc seconds to the galaxies.

In order to study the morphology and the structural properties of our sample galaxies, we additionally included in our analysis archival HST WFPC2 images in the filter F606W (HST proposal ID 11107, P.I: T. Heckman), which are also presented in Figure 1 as insets. These images reveal the complex morphology of the inner, high surface brightness regions of these GPs, and will be used for discussion in Section 4.2.

2.2.2. GTC spectroscopy

Long-slit spectroscopy was carried out in the standard mode (2×2 binning) with the highest resolution mode available at these dates, $R \sim 1018$ (at 5510\AA) and $R \sim 1122$ (at 7510\AA). Thus, we used the R1000B and R1000R grisms and a slit width of 0.8 arcsec, projecting onto a full width at half maximum (FWHM) of about 3 pixels. This setup yields wavelength coverages in the blue ~ 3630 – 7500\AA and in the red ~ 5100 – 10250\AA , with typical dispersion values of 2.1 and 2.6\AA pixel^{-1} , at 5510\AA and 7510\AA respectively. The spectra were taken along the parallactic angle. For each galaxy, blue and red spectra were taken during different (dark) nights. Seeing conditions varied between 1 and 1.4 arcsec, while atmospheric conditions were also not uniform, being two of the nights spectroscopic, three of them clear, and the remaining night slightly cloudy. Some Saharian dust was present in the atmosphere, affecting those observations at lower air masses significantly, reducing their final S/N, and doing more difficult the sky-background subtraction. This is more evident in the red part of the spectra, where large sky residuals are present. Noisiest regions in the blue and red ends of the observed spectral range were not considered in the subsequent analysis. A series of bias, twilight sky and dome flats, two calibration lamps, as well as one or two spectrophotometric

¹Detailed information on GTC and OSIRIS can be found in <http://www.gtc.iac.es>

standards were observed during the same nights.

2.2.3. Data reduction

The data were fully reduced and calibrated using IRAF² routines. This includes the usual procedures for bias and overscan subtraction, flat-fielding corrections, cosmic ray removal, and co-addition. For the broad-band images, additional large scale illumination and fringing patterns were removed effectively after subtraction of a “master sky” frame. This was obtained combining the 5x5 dithered science frames (after standard corrections and masking-out all saturated stars in the field) of each object. Finally we got deep ($\mu_z \sim 26\text{--}27$ mag arcsec⁻²) images after a good sky-background subtraction. For the spectra, wavelength calibration was done using HgAr+Xe+Ne lamp arcs. The accuracy ($\lesssim 0.1\text{\AA}$) was checked *a posteriori* using sky emission lines. The spectra was corrected for atmospheric extinction and then flux calibration was performed using several spectrophotometric standards (Grw70+8247, Ross640, L1363-3, G157-34) along the observing blocks, taken at the same night for each grating.

3. GTC SPECTROSCOPY: ANALYSIS AND RESULTS

In Figure 2 we present the OSIRIS-GTC spectra for the three GPs. The spectra are dominated by intense narrow nebular emission lines on top a faint blue stellar continuum lacking stellar Balmer absorption features. The high S/N of spectra allowed for a detection of several faint emission lines (e.g. the temperature-sensitive [OIII]4363 line) that are displayed magnified in the lower panel.

3.1. Emission-line intensities and reddening correction

We measured emission line intensities on the reduced and calibrated spectra of the three galaxies using the task `splot` of the package IRAF. To measure the flux of a given line, we integrated the flux between two points given by the position of a local continuum placed by eye. The statistical

errors associated with the measured emission line fluxes were calculated using the following expression (Pérez-Montero & Díaz 2003):

$$\sigma_i = \sigma_c \sqrt{N + \frac{W_i}{\Delta}}$$

where σ_i is the error flux of the measured emission line, σ_c is the *rms* error derived for the local continuum, N is the number of pixels taken for the measurement of emission line flux, W_i is the absolute value of the emission line equivalent width, and Δ is the wavelength dispersion. Although there is absorption of the Balmer emission lines caused by underlying stellar populations in the objects (Díaz 1988), we checked in the residuals to the STARLIGHT fitting (see § 3.3) that this effect is negligible compared to the reported errors. The emission line fluxes, $F(\lambda)$, relative to $F(\text{H}\beta) = 1000$, are listed with their corresponding errors in Table 3.

Each emission line flux is affected by the presence of interstellar dust which absorbs it according to the law:

$$\frac{I(\lambda)}{I(\text{H}\beta)} = \frac{F(\lambda)}{F(\text{H}\beta)} 10^{-c(\text{H}\beta)f(\lambda)}$$

where $I(\lambda)$ and $F(\lambda)$ are the corrected and measured emission line fluxes, respectively, $c(\text{H}\beta)$ is the constant of reddening, and $f(\lambda)$ is the extinction law, which for this work, we took from Cardelli, Clayton, & Mathis (1989), and whose values are also listed in Table 3 for the corresponding listed emission lines. $c(\text{H}\beta)$ was calculated for each object as the error-weighted least square fit to the relation between the extinction law and the quotient between the observed-to-theoretical Balmer and $\text{H}\beta$ emission line fluxes before and after underlying continuum subtraction. We found that the differences between the corrected and uncorrected $c(\text{H}\beta)$ values are always smaller than the uncertainties quoted in Table 3. The Balmer emission-lines with enough S/N reach up to H17 for GP004054, H11 for GP113303, and H15 for GP232539. The theoretical emission-line ratios were derived using Storey & Hummer (1995) values for the appropriate electron density and temperature for each one of the three galaxies. Taking the three objects coordinates into account to calculate the corresponding Galactic extinction,

²IRAF: the Image Reduction and Analysis Facility is distributed by the National Optical Astronomy Observatories, which is operated by the Association of Universities for Research in astronomy, Inc. (AURA) under cooperative agreement with the National Science Foundation

which are $c_g(\text{H}\beta) = 0.09$ for GP004054, 0.02 for GP113303, and 0.05 for GP232539, we conclude that the dominant contribution to reddening is due to intrinsic extinction. The extinction-corrected emission line fluxes relative to $I(\text{H}\beta) = 1000$, along with their corresponding errors are listed in Table 3. In this table we also list the respective constants of reddening, the extinction corrected $\text{H}\beta$ flux and the $\text{H}\beta$ equivalent widths.

3.2. Electron densities and temperatures

All physical conditions, including electron density and temperature, were calculated using the task `temden` of the package IRAF, taking for each species the same atomic coefficients as in Hägele et al. (2006). All of them, as described in this subsection, are listed in Table 4.

Electron density has been estimated by taking the emission-line ratio of $[\text{SII}]$ 6716, 6731 Å. The error propagation from the emission-line fluxes does not allow to give a precise estimate of the density in any of the three galaxies, but it gives in all cases an upper limit which is much lower than the critical density for collisional deexcitation.

Electron temperature of $[\text{OIII}]$ was derived with high precision in the three galaxies by taking the emission line ratio between the sum of 4959, 5007 Å and 4363 Å. This gives temperatures for the three objects which are typical for BCDs and HII galaxies (Campbell et al. 1986; Masegosa et al. 1994; Izotov et al. 2006; Kehrig et al. 2006; Hägele et al. 2006, 2008), ranging from 13400 K for GP004054 and 14600 K for GP232539.

Other electron temperatures than $[\text{OIII}]$ were not derived directly in any of the three objects. Although $[\text{OII}]$ 7319, 7330 Å and $[\text{NII}]$ 5755 Å were detected in the spectra of the galaxies, they did not lead to a precise derivation of the corresponding electron temperatures. Therefore, in order to calculate the corresponding ionic abundances, we derived these temperatures from $t_e([\text{OIII}])$ and using the expressions obtained from photoionization models described by Pérez-Montero & Díaz (2003) and Pérez-Montero & Contini (2009) for $t_e([\text{OII}])$ and $t_e([\text{NII}])$, respectively. Regarding $t_e([\text{SIII}])$, as the nebular lines at 9069, 9532 Å have not been detected, we derived this temperature again from $t_e([\text{OIII}])$, but using the empirical relation obtained by Hägele et al. (2006). These derived

temperatures are also listed in Table 4.

3.3. Ionic and total chemical abundances

Ionic abundances were calculated for the visible chemical species in our optical spectra by using the task `ionic` of the IRAF package and taking the same atomic coefficients described in Hägele et al. (2006) and the corresponding ionization correction factors (ICF). The ionic and total abundances, along with these ICFs are listed in Table 4.

Helium abundances³ have been obtained assuming that

$$\frac{\text{He}}{\text{H}} \approx \frac{\text{He}^+ + \text{He}^{2+}}{\text{H}^+}$$

He^+ abundances (noted as y^+ in Table 4) were calculated as the error-weighted mean of the abundances derived using the HeI emission lines at 4471, 5876, 6678 and 7065 Å, with $t_e([\text{OIII}])$ and taking the expressions described by Olive & Skillman (2004). Only in the case of GP113303 we measured the HeII nebular emission line, but the corresponding y^{2+} abundance is negligible as compared to y^+ . The derived He abundances (denoted as y in Table 4) range from 0.087 to 0.089. These values fall between the pre-galactic He/H ratio of 0.08 (Luridiana et al. 2003) and the solar ratio 0.10 (Lodders 2003), and are “normal” for low-metallicity star-forming galaxies (e.g., Kobulnicky & Skillman 1996; Hägele et al. 2008).

Oxygen abundances were calculated assuming that

$$\frac{\text{O}}{\text{H}} \approx \frac{\text{O}^+ + \text{O}^{2+}}{\text{H}^+}$$

with O^+ abundances derived from the $[\text{OII}]$ 3727 Å emission line and taking $t_e([\text{OII}])$. In the case of O^{2+} , we took $[\text{OIII}]$ 4959, 5007 Å emission line intensities with $t_e([\text{OIII}])$. The oxygen total abundances, ranging from $12 + \log(\text{O}/\text{H}) = 7.81$ for GP232539 to 7.98 for GP004054, are \sim one fifth solar $[12 + \log(\text{O}/\text{H})]_{\odot} = 8.69$, Asplund et al. (2009)].

Nitrogen abundances were calculated by assuming:

³No correction by neutral Helium nor by collisional excitation have been considered

$$\frac{N}{H} \approx ICF(N^+) \cdot \frac{N^+}{H^+}$$

and deriving N^+ abundances from the [NII] 6548, 6584 Å emission-line fluxes and $t_e([NII])$. The ICF was calculated using the expression described in Pérez-Montero & Contini (2009). The derived N/O ratios, ranging from $\log(N/O) = -0.99$ for GP232539 to -1.06 for GP004054, are well above the typical values corresponding to star-forming galaxies of the similar metallicity, i.e., the N/O plateau seen at $\log(N/O) \sim -1.5$, (e.g., Izotov & Thuan 1999).

Neon abundances were calculated by assuming:

$$\frac{Ne}{H} \approx ICF(Ne^{2+}) \cdot \frac{Ne^{2+}}{H^+}$$

calculating Ne^{2+} ionic abundances from [NeIII] 3868 Å with $t_e([OIII])$, and using the expression for the corresponding ICF described by Pérez-Montero et al. (2007). The derived Ne/O ratios are all slightly higher than the solar value [$\log(Ne/O)_\odot = -0.76$, Asplund et al. (2009)].

Argon chemical abundances were calculated in GP004054, for which both [ArIII] 7136 Å and [ArIV] 4740 Å were measured, and in GP232539, with the [ArIII] 7136 Å emission line. Then, since we have both ionic argon abundance Ar^{2+} and Ar^{3+} in GP004054, and only the first one, Ar^{2+} , in GP232539, different ICFs were considered according to the expressions proposed by Pérez-Montero et al. (2007). As in the case of neon, both argon-to-oxygen ratios result higher than the solar value [$\log(Ar/O)_\odot = -2.29$, Asplund et al. (2009)].

Sulphur abundance was calculated by assuming the following:

$$\frac{S}{H} = ICF(S^+ + S^{2+}) \cdot \frac{S^+ + S^{2+}}{H^+}$$

with the S^+ derived from the [SII] 6717, 6731 Å and assuming that $t_e([SII]) \approx t_e([OII])$. In the case of S^{2+} , since our available spectral range has not allowed a measurement of the [SIII] emission lines at 9069, 9532 Å, we derived their ionic abundances with [SIII] 6312 Å, and with $t_e([SIII])$. We considered the ICF for $(S^+ + S^{2+})$ obtained by Pérez-Montero et al. (2006). The derived sulfur-to-oxygen ratios range from -1.22 for GP113303

to -1.55 for GP232539. The high quoted errors for S/O make the derived values to be consistent with the solar value [$\log(S/O)_\odot = -1.57$, Asplund et al. (2009)].

Finally, iron abundance was calculated from Fe^{2+} with the emission line relative intensity of [FeII] 4658 Å and the electron temperature of [OIII]. We have also used the ICF proposed by Rodríguez & Rubin (2004). All Fe/O are similar in the three galaxies, ranging from -1.49 for GP004054 to -1.69 for GP232539.

The derived Ne/O, S/O, Ar/O, and Fe/O values (see Table 4) are, within uncertainties (which are especially high for S/O and Fe/O), consistent within the three galaxies. Overall, their values can be considered as “normal” when compared to the mean values found for nearby BCDs and HII galaxies in the literature (e.g., Izotov & Thuan 1999; Hägele et al. 2006, 2008).

3.4. Spectral fitting

In order to gain insights into the SFH of the GPs under study, we interpreted their integrated spectra by means of spectral synthesis models. To check the consistency of our results, we used both the population synthesis code STARLIGHT⁴ (Cid Fernandes et al. 2004, 2005; Mateus et al. 2006) and a two-component evolutionary synthesis code that is based on PEGASE 2.0 (Fioc & Rocca-Volmerange 1997).

We used STARLIGHT to synthesize the observed stellar continuum of the galaxies as due to the superposition of single-age stellar populations (SSPs) of different ages and metallicities. We used the SSP library provided by the POPSTAR⁵ synthesis models (hereafter RUN 1, Mollá et al. 2009; Martín-Manjón et al. 2010, García-Vargas et al. in prep.). These models follow the evolution of SSPs from very young (0.1 Myr) to very old (15.8 Gyr) ages by combining Padova '94 stellar evolution models with the most recent physics for stellar atmospheres and nebular continuum emission. POPSTAR models are therefore particularly

⁴The STARLIGHT project is supported by the Brazilian agencies CNPq, CAPES and FAPESP and by the France-Brazil CAPES/Cofecub programme. <http://www.starlight.ufsc.br>.

⁵POPSTAR models are publicly available from <http://www.fractal-es.com/PopStar/SEDmod.html>

well suited for the modeling of star-forming galaxies (Mollá et al. 2009). Note that the low spectral resolution (20 Å) of the currently available POPSTAR SSPs does not permit a perfect match to Balmer stellar absorption features. This, however, is not expected to have a notable impact on the derived SFHs.

In low-metallicity starburst galaxies, a significant contribution from nebular continuum emission is expected to be superimposed upon the stellar SED. The gaseous emission not only enhances the luminosity of the galaxy but it additionally tends to make its spectral continuum redder than what is expected from a stellar SED (e.g., Krueger et al. 1995; Papaderos et al. 1998, Iz11). Therefore, as recently pointed out by Iz11, if nebular continuum emission is not taken into account in SED fitting for starburst galaxies the estimated stellar masses can be severely overestimated. In this respect, the new POPSTAR SSPs including nebular continuum and line emission offer an important advantage towards a realistic SED modeling of GPs.

In modeling the stellar SED we used SSPs with three different metallicities, 0.008, 0.004, and 0.0004 (i.e., $\sim 1/2$, $1/5$, and $1/45$ solar) for a Kroupa initial mass function (IMF) between 0.15 and 100 M_{\odot} , and all available SSPs between $\log t = 5.0$ -10.2 yr. For the SSPs with the youngest ages, i.e., ≤ 20 Myr, we only used models with $Z = 0.004$, which is the closest value to the gas-phase metallicity that we determined (see Table 3) whereas for the older stellar component all three available metallicities were used. Prior to STARLIGHT models, the flux calibrated spectra were de-redshifted and resampled to 1 Å/pixel. Spectral regions with strong emission lines or sky-subtraction residuals were masked out from fitting. Models were applied on the wavelength range 3500–6700 Å (rest frame) to exclude noisy spectral regions. The S/N ratio of the spectra in the relatively featureless window between 4220 and 4280 Å varies from 15 to 45 for the three galaxies.

3.4.1. run 1: POPSTAR models

The STARLIGHT fits based on the POPSTAR SSPs are shown overlaid with the observed spectra in the upper panels of Figures 3-5. It can be seen that in all cases the synthetic stellar and gaseous SED provides a good match to the obser-

vations. The right upper diagram shows the luminosity contribution (%) of the SSPs evaluated by STARLIGHT to the normalization wavelength of 4170 Å. Vertical thin-gray lines depict the ages available in the POPSTAR library. The stellar mass fraction corresponding to each SSP is plotted on the lower panel.

The main output from the STARLIGHT models for POPSTAR SSPs is summarized in Table 5. Columns 2–4 list the predicted relative contribution of the nebular emission to the total continuum emission at the [OII], H β and H α wavelengths. The obtained fraction of young (≤ 100 Myr) stars $M_{\star, \text{young}}$ with respect to the existing stellar mass of $\sim 20\%$, suggests that GP004054 currently experiences a major episode in its assembly history. The last two columns of Table 5 list the existing total stellar mass $M_{\star, \text{total}}$ and the reduced χ^2 . It is interesting to point out that the stellar mass $M_{\star, \text{total}}$ estimated from the fits, ~ 2 – $3 \times 10^9 M_{\odot}$, places GPs in the range of luminous BCDs (e.g. Bergvall & Östlin 2002; Guzmán et al. 2003), even when aperture corrections (cf. Sect. 3.4.4) are taken into account. It can be seen that the STARLIGHT solutions delineate two main SSP groups, a younger one dominating the optical light, and an older stellar component (~ 10 Gyr), contributing most ($\gtrsim 80\%$) of the stellar mass. Signatures for an intermediate-age stellar population were found for GP232539 only, where SSPs at ~ 0.25 and ~ 2.5 Gyr appear to make a substantial ($\gtrsim 20\%$) contribution to the stellar mass.

Whereas the strong starburst activity in the GPs under study is obvious, already from their high emission-line EWs, the inferred mass fraction $M_{\star, \text{young}}$ of stars recently produced is to be considered with some caution. Spectral synthesis models are known to be plagued by substantial degeneracies, in particular for SFGs (see e.g. Guseva et al. 2001, for a detailed discussion) making quantitative statements on the reality and relative importance of individual features in the derived SFH difficult. Additionally, it should be called into attention that here we present a pilot attempt of using POPSTAR SSPs in conjunction with STARLIGHT and no rigorous tests of possible numerical effects in this context have been made so far.

We therefore include below two further modeling attempts in order to gauge the variation of the derived $M_{\star, \text{young}}$ for the GPs under study.

In the first one (hereafter RUN 2), we employed STARLIGHT using, however, SSPs based on the stellar models by Bruzual & Charlot (2003). One of the main differences between POPSTAR and Bruzual & Charlot models is the inclusion of nebular continuum emission in the former (a detailed comparison of POPSTAR and other models can be found in Mollá et al. (2009)). Additionally, the Bruzual & Charlot SSPs have a higher spectral resolution and assume a Salpeter IMF between 0.1 and 100 M_{\odot} .

3.4.2. run 2: $B\&C$ models

For RUN 2 (lower panels of Figures 3-5) we imposed roughly the same constraints as for RUN 1, using the same masks for emission lines (shaded areas) and normalization wavelength, and an SSP library with nearly the same age and metallicity coverage. The main results as derived from RUN 2 are also included in Table 5. Comparing them with those from RUN 1, we found a satisfactory agreement in the overall SSP age distribution, with two prominent peaks at young and old ages for GP113303 and signatures of an additional intermediate-age stellar population in GP004054 and GP232539. In view of the differences in the SSP libraries and the details of the SFH obtained, some differences in, e.g., total stellar mass and young stellar mass fraction obtained from RUN 1 and 2 are not surprising. With the exception of GP004054, RUN 1 yields a significantly lower total stellar mass and a higher mass fraction from young stellar populations by a factor of about 2 (~ 0.3 dex) compared with those obtained from RUN 2 (see Table 5).

3.4.3. run 3: evolutionary synthesis models

As a second consistency check (RUN 3), we applied a modified version of the evolutionary synthesis code PEGASE 2.0 (Fioc & Rocca-Volmerange 1997). In this approach, each spectrum was modeled as due to the superposition of the SED from an old and a young stellar population approximating, respectively, the underlying host galaxy and the starburst component. The host was modeled by an exponentially decreasing SFR since 13 Gyr with an e-folding time of 3 Gyr. Note that the assumed SFH for the host implies for GP004050 and GP113303 some contribution from intermediate-age to young (0.1–1 Gyr) stars

which is not apparent from the STARLIGHT fits (RUN1&2). As for the young stellar component, we assumed an instantaneous burst whose age was allowed to vary between 0 and 50 Myr. The SEDs were computed assuming a fixed stellar metallicity of $Z_{\odot}/5$ and a Salpeter IMF (0.1–100 M_{\odot}), and include nebular continuum and line emission.

The best-fitting solutions were constrained by varying the burst age, extinction $C(H\beta)$ and burst parameter b_{par} (mass fraction of stars formed in the burst with respect to the mass of the stars ever formed) that reproduce best the observed SED continuum and $H\alpha$ and $H\beta$ EWs. We note that the concept used here, i.e. the exploration of the SFH and $C(H\beta)$ that self-consistently account for Balmer line EWs, in addition to stellar SEDs and colors of SFGs was originally used for specific tasks in Izotov et al. (1997) and Papaderos et al. (1998) and further developed in Guseva et al. (2001) and Guseva et al. (2007).

In the lower panels of Figures 3-5 we show the best-fitting SEDs for the young and the old stellar component as blue and red shaded areas, respectively. It can be seen that the superposition of a burst on an evolved galaxy host (black curve) can reproduce quite well the spectra of GP004054 and GP232539, whereas some systematic deviations are present in the case of GP113303. This might be attributed to the absence of an intermediate-age population in the latter system, as revealed by the STARLIGHT models in RUN 1&2. The relevant model output is summarized in Table 6. Interestingly, in all cases the best-fitting models imply an $C(H\beta)$ very close to the measured value for the nebular component. They also yield a good match to the observed $H\alpha$ and $H\beta$ EWs.

Tables 5 & 6 show the significant variation of certain parameters (e.g. $M_{\star, \text{young}}$) over RUN 1 through RUN 3. While they may not be surprising in view of the different models, SSP libraries and fitting constraints used, they reflect the inherent uncertainties in the reconstruction of the SFH of individual starburst galaxies using state-of-art spectral synthesis models. On the other hand, it is worth pointing out that all models, especially those including nebular emission (RUN 1 and RUN 3), consistently suggest that our sample GPs presently undergo a significant evolutionary stage in which they rapidly form between a few % and up to $\sim 20\%$ of their stellar mass. This high-

lights the importance of these objects as laboratories for studying galaxy evolution at late cosmic epochs.

3.4.4. Aperture corrections

We did not applied any aperture correction before fitting our spectra. However, our flux calibration was checked using the SDSS spectra and SDSS broad-band magnitudes. We calculated the fraction of total optical light covered by the OSIRIS long-slit, deriving a slit coverage a factor of 1.5–1.8 smaller than those of the SDSS fiber. According to the fraction of light inside the SDSS fiber calculated in A10, we estimated a slit coverage of about 45–55% of the visible light in the SDSS images. Therefore, we must keep in mind that all global properties that can be derived from the spectral analysis (e.g., stellar mass) may be lower than their true values.

3.5. Wolf-Rayet features

All massive ($M \geq 25 M_{\odot}$ for Z_{\odot}), very luminous ($10^5 - 10^6 L_{\odot}$) O stars pass through the WR phase 2–5 Myr after their birth, spending less than 5×10^5 yr in this phase (e.g. Schaerer & Vacca 1998, Meynet & Maeder 2005). The presence of WR stars, as often observed in extragalactic HII regions (Gonzalez-Delgado et al. 1994; Garcia-Vargas et al. 1997), and in both integrated (e.g., Allen et al. 1976; Kunth & Sargent 1981; Conti 1991; Masegosa et al. 1991; Vacca & Conti 1992; Schaerer et al. 1999; Guseva et al. 2000; Brinchmann et al. 2008) and spatially resolved (Kehrig et al. 2008; Monreal-Ibero et al. 2010; López-Sánchez et al. 2011) spectra of starburst galaxies, is characterized by the detection of two broad emission features in their optical spectra. One of these features is the blue WR bump, which is a blend of the NIII $\lambda 4640$, CIII/CIV $\lambda 4650$, and the broad HeII $\lambda 4686$ emission line. This feature is mainly due to WN stars. In contrast, WC stars are the main responsible for the red WR bump, which is a blend of the CIII $\lambda 5698$ and CIV $\lambda 5808$ broad emission lines. The red WR bump is weaker than the blue one and is rarely observed at low metallicities (Crowther 2007). WR stars are present in galaxies with recent starbursts (e.g., BCDs, Guseva et al. 2000; Pérez-Montero et al. 2010). In GPs, however, no WR features had been detected so far.

Figure 6 shows a zoom of the OSIRIS spectra in the 4200Å–5200Å (rest-frame) range, where the blue WR bump is detected in the three GPs. These WR features are also identified after the subtraction of the continuum fitting by STARLIGHT. In contrast, none of the galaxies has a red bump detection.

Given the low spectral resolution of our data, we measure the WR bumps by using the IRAF task `splot`. First, we fitted and subtracted the adjacent continuum. Then we fitted gaussians to the nebular emission lines in the region between 4600 and 4750Å, and finally we integrated the remaining emission above zero to have an estimate of the blue WR bump fluxes. The main properties derived from these measurements are summarized in Table 6. For example, from the luminosity of the bump, and adopting a theoretical WR luminosity from STARBURST99 models (Leitherer et al. 1999) at the same metallicity, we inferred the number of WR stars expected for each galaxy.

4. DISCUSSION

4.1. Stellar mass

In Table 5 we list stellar masses contained in the spectroscopic aperture as derived from the spectral fitting, and using the adopted distances to the galaxies (see Table 1), and mass-to-light ratios obtained from the mixture of POPSTAR synthetic stellar populations fitted to each galaxy spectrum. We also give in Table 5 an estimate of the percentage of the stellar mass given by stellar populations younger than 20 Myr, and the fractional contribution — for three different spectral ranges — of the nebular continuum.

Our stellar mass estimates from RUN 1 for GP004054 ($M_{\star} = 1.7 \times 10^9 M_{\odot}$), GP113303 ($M_{\star} = 2.8 \times 10^9 M_{\odot}$), and GP232539 ($M_{\star} = 2.4 \times 10^9 M_{\odot}$), confirm that these galaxies are *dwarfish systems* having had formed between a few % and up to $\sim 20\%$ of their present stellar mass in a recent (≤ 100 Myr) major star formation episode. Note that the stellar masses derived here are not far from those inferred for the same objects in previous studies (see Table 1), despite significantly different modeling approaches used.

Discrepancies are likely due to the inclusion of the contribution of the nebular continuum emission (RUN 1) in this study. For the three analyzed

objects, we find this contribution to be significant and to increase to several % towards the red spectral range (see Table 5). The impact of the red nebular continuum on SED fitting is already suggested by the fact that STARLIGHT models based on purely stellar SSPs (RUN 2) yield a by a factor ~ 2 lower $M_{\star, \text{young}}$, consequently a larger mass fraction of old stars. Precisely this effect was discussed by Iz11 and invoked in order to explain the differences between their M_{\star} values and those derived by C09 for the whole sample of GPs. Note, however, that we do not find any clear correlation between the offset of the derived stellar masses and the relative flux contribution of the nebular continuum in our three studied objects.

For GP004054, C09 and Iz11 did not published M_{\star} values. However, we compared our estimates with those given by Overzier et al. (2009). The latter were obtained from the SDSS/DR7 stellar mass catalog⁶, and derived using SDSS photometry and a large grid of models constructed on the basis of the Bruzual & Charlot (2003) library. Interestingly, stellar masses calculated here for GP004054, and also for GP113303 and GP232539 (also listed by Overzier et al. (2009)) are within ~ 0.3 dex in agreement with our values. It is worth noting that values given by Overzier et al. (2009) did not take into account any contribution from nebular continuum, which may be possibly masked or compensated by other uncertainties.

4.2. The star formation history of the GPs

Several constraints on the SFH of the studied GPs can be inferred from our results. As consistently indicated by spectral synthesis models, none of them presently forms its first stellar population. Quite to the contrary, an evolved stellar component with an age between a few 10^8 yr and several Gyr is present in all three GPs and provides at least $\sim 80\%$ of their stellar mass. In particular, direct evidence for an old stellar component is found for the system GP113303, where we detect a faint ($EW \sim 1.5\text{\AA}$) but clear $\text{MgI}\lambda\lambda 5167, 5173$ broad absorption line. This feature is due to the presence of old stars and, as shown in Fig 7, it is clearly visible by eye in the spectra. At least for GP113303, the detection of this feature gives us the confir-

mation of the presence of old stars. Whereas for GP004054 and GP232539 the spectral fitting led to similar results than for GP113303, absorption features in their spectra are probably too faint to be detected.

Both population and evolutionary synthesis models including the nebular component (RUN 1&3) imply, on the other hand, that the GPs studied here are experiencing a significant stage in their buildup, as they form $\sim 4\text{--}20\%$ of their total mass in an intense intermittent or prolonged starburst episode which, as suggested by the presence of WR features is very recent or still ongoing.

The strong starburst ($\text{SFR} \sim 7 - 14 M_{\odot} \text{ yr}^{-1}$, see Table 1) taking place in these galaxies and their low stellar masses ($\sim 1.5 - 2.7 \times 10^9 M_{\odot}$ yr^{-1}) imply large *specific* star formation rates, $\text{sSFR} \sim 2 - 9 \times 10^{-9} \text{ yr}^{-1}$. In agreement with C09 and Iz11, these values are typical for GPs but they are unusually high in the local Universe (Brinchmann et al. 2004), being more comparable to those observed in high redshift starburst galaxies. Since these sSFRs imply relatively short mass doubling times ($\equiv 1/\text{sSFR}$) $\lesssim 500$ Myr, it is likely that the GP evolutionary stage is very brief. This is also to be expected from the enormous energetic release from the starburst that will quickly heat up and disperse the cold gas reservoir of GPs, quenching star-forming activities after a few Myr. The starburst nature of GP is also supported by STARLIGHT fits which suggest longer quiescent phases preceeding the current burst ranging from a few 10^8 yr in the case of GP232539 to $\sim 1\text{--}10$ Gyr for GP004054 and GP113303. Note that the smoother SFH of GP232539, resulting into a substantial intermediate-age stellar component is indicated by both RUN 1 and RUN 2.

The overall evidence (stellar mass, SFH pattern and burst parameter) is consistent with the hypothesis of GPs being identifiable with previous starburst-dominated phases in the lifetime of luminous BCDs in the local Universe. As apparent from HST/WFPC2 *R*-band (F606W) images (Fig. 1), the GPs under study are as well compatible to local BCDs with respect to their compactness (~ 5 kpc) and the irregular morphology of their high-surface brightness component. Furthermore, similar to what is found for the main population of chemically evolved ($7.6 \lesssim 12 + (\text{O}/\text{H}) \lesssim 8.3$) nearby BCDs (e.g., Papaderos et al. 1996; Cairós

⁶Available at <http://www.mpa-garching.mpg.de/SDSS/DR7/>.

et al. 2001, 2003; Noeske et al. 2003; Gil de Paz & Madore 2005; Vaduvescu et al. 2006; Corbin et al. 2006; Amorín et al. 2007, 2009), the GPs studied here show a more extended lower-surface brightness (LSB) envelope that is presumably due to an old stellar host. It is worth pointing out, on the other hand, that, contrary to most BCDs, the LSB host of GPs displays significant departures from ellipticity, suggesting a lesser degree of dynamical relaxation, or merger origin, which appears rather typical for the high-luminosity end of local BCDs (e.g. Telles et al. 1997; Östlin et al. 2001; Bergvall & Östlin 2002; Adamo et al. 2011). This is particularly true for GP113303 for which HST data reveal significant LSB emission out to ~ 10 kpc southwest of its nuclear region.

The properties of the LSB component can be better quantified from the surface brightness profiles (SBPs) in Fig. 8. The SBPs were derived using method iv in Papaderos et al. (2002) and were converted to the Vega system, following the prescriptions by Holtzman et al. (1995). They have been corrected for cosmological dimming as $\mu_{\text{corrected}} = \mu_{\text{observed}} - 10 \log(1+z)$ and for Galactic extinction but no k corrections were applied. It can be seen that all SBPs show an outer exponential intensity decrease in their LSB envelope, as is typically the case for nearby BCDs. On the assumption that the LSB emission is of stellar origin, one can infer from linear fits to the exponential part of the SBPs the scale length and central surface brightness of GP hosts to 1.5–3 kpc and 19–21.5 mag arcsec $^{-2}$, respectively. In Fig. 9 we compare the structural properties of the host galaxy of GPs with those of local BCDs, dwarf irregulars (dIs), LSB galaxies and dwarf ellipticals (dEs). It can be seen that GPs fall in the parameter space that is populated by luminous BCDs, indicating that these two galaxy classes are very similar structurally.

One word of caution is in order here. A roughly exponential intensity drop off is a generic property of extended nebular halos that are expected to arise in galaxies with strong starburst activity (Papaderos et al. 2002). An exponential profile in the LSB periphery of GPs should not therefore be taken as a foolproof sign of an extended *stellar* host galaxy. If the LSB envelope is partly or entirely due to extended nebular emission, then the absolute magnitude of the GP host will decrease

by 0.75–1 mag, with a simultaneous brightening of the central surface brightness and decrease of the exponential scale length. This would move the GPs under study downstream in either plot, in better agreement to lower-luminosity BCDs.

4.3. The nitrogen over-abundance in GPs

The good quality of the GTC data allowed us to derive the physical properties and chemical abundances of the ionized gas in the sample GPs with much better accuracy than previously done for these galaxies.

The derived electron temperatures and densities ($T_e(\text{[O III]}) \sim 13000\text{--}15000$ K, $n_e(\text{[S II]}) < 600$ cm $^{-3}$) are consistent to those measured by A10 and by Iz11 for a larger sample of GPs. Moreover, these values are in general agreement with those typically measured in other samples of nearby star-forming dwarf galaxies (e.g., Campbell et al. 1986; Masegosa et al. 1994; Lee et al. 2004; Hägele et al. 2008).

The oxygen abundances ($12+\log(\text{O/H})$) found for the sample GPs are 7.81 ± 0.14 , 7.91 ± 0.10 , and 7.98 ± 0.06 for GP232539, GP113303, and GP004054 respectively. These metallicity values are also consistent with those previously published using SDSS data (see Table 1), and confirm that the three GPs are *metal-poor galaxies*.

On the other hand, the three GP galaxies appear to be relatively *rich in nitrogen*. The logarithmic N/O ratios determined for the sample GPs are -1.06 ± 0.04 , -1.04 ± 0.08 , and -0.99 ± 0.11 for GP004054, GP113303, and GP232539, respectively. These values are slightly higher (0.2 dex on average) than those previously obtained by A10. Differences can be attributed to large differences in S/N between GTC and SDSS spectra. Moreover, it is worth noting that in the calculation of the nitrogen abundance we took into account the $[\text{N II}]\lambda 6548\text{\AA}$, which is clearly detected in the GTC spectra and mostly undetected in the SDSS spectra. The three GP galaxies studied here show N/O ratios that are clearly higher than the usual upper limits of the *plateau* on the N/O vs. O/H diagram and more compatible with those of emission-line galaxies with higher metallicities and similar sSFR (e.g., Mallery et al. 2007) for which secondary nitrogen production takes over. Using a large sample of galaxies that include the

GPs of C09, Iz11 noticed that for galaxies with $\text{EW}(\text{H}\beta) < 100\text{\AA}$ there is a dependence of the N/O ratio on the total galaxy mass, implying some secondary nitrogen production in the highest-mass galaxies ($\gtrsim 10^9 M_\odot$, see their Fig. 12).

In order to explain the observed high N/O ratios in metal-poor SFGs several mechanisms, including time delays on chemical enrichment, effects of gas flows, and variations in the SFHs (e.g., recurrent bursts) have been proposed in the literature (see e.g., Garnett 1990; Pilyugin 1992; Köppen & Edmunds 1999; van Zee & Haynes 2006; Mollá et al. 2006; Pilyugin et al. 2012). Using a large sample of metal-poor emission-line galaxies, Izotov et al. (2006) found an apparent increase of N/O with decreasing $\text{EW}(\text{H}\beta)$, best seen at intermediate metallicities. They interpreted this trend as an evidence of gradual enrichment of the HII regions in nitrogen by massive stars from the most recent starburst. In this line, the discovery of WR stars in the three GPs studied here offer additional ingredients to the discussion.

Localized chemical pollution by WR stars has been argued to explain the enhancement in nitrogen abundance in the central starburst of nearby WR galaxies (e.g., NGC5253 Kobulnicky & Skillman 1997; López-Sánchez et al. 2007, 2011; James et al. 2009; Monreal-Ibero et al. 2010). These regions, with sizes of about tenths of parsecs usually show N/O enhancements consistent with few WRs stars (Monreal-Ibero et al. 2010). In their integrated spectra, most WR galaxies with $\text{EW}(\text{H}\beta) \lesssim 100\text{\AA}$ in Brinchmann et al. (2008) (see also López-Sánchez & Esteban 2010) show higher N/O than non-WR galaxies, suggesting a rapid enrichment by WR stars. However, most of these WR galaxies with N/O values comparable to our GPs show much higher oxygen, neon, and argon abundances at the same $\text{EW}(\text{H}\beta)$ (see their Fig. 15). Helium abundances in the three GP galaxies are roughly the same and not especially high. Indeed, these values are comparable to those found in most BCDs (e.g., Pagel et al. 1992). As pointed out by Pagel et al. (1986, 1992) (see also Kobulnicky & Skillman (1997)) high He/H ratios are to be expected in regions with strong WR pollution. However, as remarked by Brinchmann et al. (2008), following results found in Galactic ring nebulae by Esteban et al. (1992), the expected average increase in He/H could be up to 0.7 dex lower than

the expected increase in N/O. So the apparently normal He/H seen in the GPs may not give additional clues in this respect.

Finally, recent results from integral field spectroscopy on three (HS 0128+2832, HS 0837+4717 and Mrk930) nitrogen overabundant BCDs by Pérez-Montero et al. (2011), have shown that these galaxies display high N/O, which are constant at spatial scales of the order of several kpc. Interestingly, their N/O values are rather similar to those of our target GPs. Pérez-Montero et al. show the evolution of N/O with time for spherical gaseous distributions of constant density with initial $12+\log(\text{O}/\text{H})=8$ and $\log(\text{N}/\text{O})=-1.6$, which is polluted by the stellar winds coming from stellar clusters with $Z = 0.004$ and different stellar masses (from 10^7 to $10^{10} M_\odot$). Importantly, their results show clearly that the number of WR stars estimated from spectroscopy cannot be responsible for the observed enhancement in the N abundance across the observed spatial scales. According to their results, in the case of the GPs it would be necessary ionizing clusters with masses 2 or 3 orders of magnitude higher to reach such degree of pollution in the spatial scale covered by our spectral aperture (see §3.3.1). This suggests that another chemical evolution scenario is required to explain the observed properties of the GPs.

One possibility is to think our galaxies as (chemically) evolved enough to have reached the secondary nitrogen regime. Köppen & Hensler (2005) used models to investigate the chemical evolution of galaxies during an episode of massive and sudden accretion of metal-poor gas due to, e.g., interaction with gas clouds or small gas-rich companions. In galaxies that has reached the secondary nitrogen regime a rapid decrease of the oxygen abundance can be produced during the infall, remaining the N/O unchanged, before a slower evolution which leads back to the closed-box relation. This theoretical model and similar results from numerical simulations (e.g., Finlator & Davé 2008) led to A10 to suggest a scenario where the GPs would be experiencing the immediate effects of a recent, massive accretion of metal-poor gas (from the galaxy outskirts or beyond), possibly modulated by enriched outflows. This, at the same time, appears consistent with the SFH and observed morphology of the GP galaxies.

5. Summary and final remarks

In this paper, we have presented for the first time deep optical broad-band imaging and spectroscopy for a sample of three GPs with a 10m-class telescope, the GTC.

Chemical abundances and physical properties of the ionized gas were derived with high precision in the three galaxies, confirming previous findings. In particular, our results support several of the conclusions drawn by A10: We find that these galaxies are metal poor ($7.8 \lesssim 12 + \log(\text{O}/\text{H}) \lesssim 8.0$) just like nearby BCDs. However, in contrast to most BCDs, the studied GPs show a remarkably high N/O ratio for their low oxygen abundance. This is in agreement with previous work by A10 (see also Pilyugin et al. 2012) who claimed after a re-analysis of SDSS data for the C09 sample of GPs that a significant fraction of these systems shows enhanced nitrogen abundances.

The high S/N GTC spectra allowed to discover clear signatures of WR stars in the three galaxies. One of the implications of this finding is that these WR stars might produce a localized chemical pollution, and therefore explain the apparent nitrogen over-abundance of the galaxies. However, by comparing with similar results for BCDs presented by Pérez-Montero et al. (2011), the derived ratio between WR and O stars for GPs seem to be not enough to explain the apparent nitrogen over-abundance as due to local pollution by WRs.

With the aim of gaining further insight into the SFH of GPs, we carried out a pilot spectral synthesis study of these systems using the code STARLIGHT in conjunction with the new-generation SSP library POPSTAR which includes nebular emission (RUN1). As a consistency check, we additionally employed STARLIGHT with purely stellar SSPs (RUN2), as well as an evolutionary synthesis code that self-consistently accounts for Balmer emission line equivalent widths (EWs) for a simplified SFH comprising an old and a young stellar population (RUN3). The central outcome from the STARLIGHT+POPSTAR model, qualitatively confirmed through the RUN2&RUN3, is that the GPs under study currently undergo a major starburst producing between $\sim 4\%$ and 20% of their stellar mass. This result is supported by the detection, for the first time in these galaxies, of clear signatures of a significant number of WR stars in

their spectra. The derived SFH of these systems shows large discontinuities between a few 10^8 yr and several Gyr, strongly suggesting that their formation history is dominated by starbursts. However, as models imply, GPs are old galaxies having had formed most of their stellar mass several Gyr ago. The presence of an old stellar component could be directly spectroscopically verified in one of our GPs, adding further support to this conclusion. Stellar masses derived from RUN1 range between $1.7 \times 10^9 M_\odot$ and $2.7 \times 10^9 M_\odot$, they are thus fairly comparable to those of luminous BCD galaxies in the nearby Universe. Moreover, a surface photometry study based on HST data indicates that our sample GPs possess an extended low-surface brightness (LSB) envelope that, if due to stellar emission, has structural properties compatible to those of luminous BCDs in the nearby Universe.

Clearly, to further elucidate the evolutionary scenarios of GPs we need a better understanding of their chemical enrichment and star formation histories. In particular, it would be important to compare accurate measurements of their chemical abundances, especially nitrogen, for a larger sample of GPs with chemical evolution models taking into account gas inflows and outflows. High-quality spectra with 8-10m class telescopes have been proved to be indispensable to study in detail faint spectral features and to reduce uncertainties in the analysis and interpretation of the data.

We would like to thank the anonymous referee for valuable comments and suggestions. We are very grateful to the GTC staff and, in particular, to A. Cabrera-Llaveros for their invaluable support with the OSIRIS observations and data reduction. This work has been funded by grants AYA2007-67965-C03-02, AYA2010-21887-C04-01, and CSD2006-00070: First Science with the GTC (<http://www.iac.es/consolider-ingenio-gtc/>) of the Consolider-Ingenio 2010 Program, by the Spanish MICINN. Polychronis Papaderos is supported by a Ciencia 2008 contract, funded by FCT/MCTES (Portugal) and POPH/FSE (EC).

Based on observations made with the Gran Telescopio Canarias (GTC), installed in the Spanish Observatorio del Roque de los Muchachos of the Instituto de Astrofísica de Canarias, in the island of La Palma.

*Facilities:*GTC (OSIRIS), HST (WFPC2).

REFERENCES

- Adamo, A., Östlin, G., Zackrisson, E., et al. 2011, MNRAS, 415, 2388
- Allen, D. A., Wright, A. E., & Goss, W. M. 1976, MNRAS, 177, 91
- Alloin, D., Collin-Souffrin, S., Joly, M., & Vigroux, L. 1979, A&A, 78, 200
- Amorín, R. O., Muñoz-Tuñón, C., Aguerri, J. A. L., Cairós, L. M., & Caon, N. 2007, A&A, 467, 541
- Amorín, R., Aguerri, J. A. L., Muñoz-Tuñón, C., & Cairós, L. M. 2009, A&A, 501, 75
- Amorín, R. O., Pérez-Montero, E., & Vílchez, J. M. 2010, ApJ, 715, L128
- Amorín, R. O., Vílchez, J. M., & Pérez-Montero, E., 2011, in JENAM Symposium *Dwarf Galaxies: Keys to Galaxy Formation and Evolution*, P. Papaderos, S. Recchi & G. Hensler (eds.). Lisbon, September 2010, Springer Verlag, in press
- Asplund, M., Grevesse, N., Sauval, A. J., & Scott, P. 2009, ARA&A, 47, 481
- Basu-Zych, A. R., et al. 2007, ApJS, 173, 457
- Bauer, A. E., Drory, N., Hill, G. J., & Feulner, G. 2005, ApJ, 621, L89
- Berg, D. A., Skillman, E. D., & Marble, A. R. 2011, ApJ, 738, 2
- Bergvall, N. & Östlin, G. 2002, A&A, 390, 891
- Bournaud, F., & Elmegreen, B. G. 2009, ApJ, 694, L158
- Brinchmann, J., Charlot, S., White, S. D. M., Tremonti, C., Kauffmann, G., Heckman, T., & Brinkmann, J. 2004, MNRAS, 351, 1151
- Brinchmann, J., Kunth, D., & Durret, F. 2008, A&A, 485, 657
- Bruzual, G., & Charlot, S. 2003, MNRAS, 344, 1000
- Bundy, K., et al. 2006, ApJ, 651, 120
- Campbell, A., Terlevich, R., & Melnick, J. 1986, MNRAS, 223, 811
- Cairós, L. M., Vílchez, J. M., González Pérez, J. N., Iglesias-Páramo, J., & Caon, N. 2001, ApJS, 133, 321
- Cairós, L. M., Caon, N., Papaderos, P., et al. 2003, ApJ, 593, 312
- Cardamone, C., et al. 2009, MNRAS, 399, 1191
- Cardelli, J. A., Clayton, G. C., & Mathis, J. S. 1989, ApJ, 345, 245
- Cepa, J., et al. 2000, Proc. SPIE, 4008, 623
- Cid Fernandes, R., Gu, Q., Melnick, J., Terlevich, E., Terlevich, R., Kunth, D., Rodrigues Lacerda, R., & Joguet, B. 2004, MNRAS, 355, 273
- Cid Fernandes, R., Mateus, A., Sodré, L., Stasińska, G., & Gomes, J. M. 2005, MNRAS, 358, 363
- Conti, P. S. 1991, ApJ, 377, 115
- Corbin, M. R., Vacca, W. D., Cid Fernandes, R., Hibbard, J. E., Somerville, R. S., & Windhorst, R. A. 2006, ApJ, 651, 861
- Cowie, L. L., Songaila, A., Hu, E. M., & Cohen, J. G. 1996, AJ, 112, 839
- Cowie, L. L., & Barger, A. J. 2008, ApJ, 686, 72
- Cresci, G., Mannucci, F., Maiolino, R., Marconi, A., Gnerucci, A., & Magrini, L. 2010, Natur, 467, 811
- Crowther, P. A. 2007, ARA&A, 45, 177
- Daddi, E., et al. 2007, ApJ, 670, 156
- Díaz, A. I. 1988, MNRAS, 231, 57
- Erb, D. K., Shapley, A. E., Pettini, M., Steidel, C. C., Reddy, N. A., & Adelberger, K. L. 2006, ApJ, 644, 813
- Esteban, C., Vílchez, J. M., Smith, L. J., & Clegg, R. E. S. 1992, A&A, 259, 629
- Finkelstein, S. L., Hill, G. J., Gebhardt, K., et al. 2011, ApJ, 729, 140
- Finlator, K., & Davé, R. 2008, MNRAS, 385, 2181

- Fioc, M., & Rocca-Volmerange, B. 1997, *A&A*, 326, 950
- Gavilán, M., Mollá, M., & Buell, J. F. 2006, *A&A*, 450, 509
- Garcia-Vargas, M. L., Gonzalez-Delgado, R. M., Perez, E., Alloin, D., Diaz, A., & Terlevich, E. 1997, *ApJ*, 478, 112
- Garnett, D. R. 1990, *ApJ*, 363, 142
- Gil de Paz, A., & Madore, B. F. 2005, *ApJS*, 156, 345
- Gilbank, D. G., et al. 2011, *MNRAS*, 402
- Gonçalves, T. S., et al. 2010, *ApJ*, 724, 1373
- Gonzalez-Delgado, R. M., et al. 1994, *ApJ*, 437, 239
- Guseva, N. G., Izotov, Y. I., & Thuan, T. X. 2000, *ApJ*, 531, 776
- Guseva, N. G., Izotov, Y. I., Papaderos, P., et al. 2001, *A&A*, 378, 756
- Guseva, N. G., Izotov, Y. I., Papaderos, P., & Fricke, K. J. 2007, *A&A*, 464, 885
- Guseva, N. G., Papaderos, P., Meyer, H. T., Izotov, Y. I., & Fricke, K. J. 2009, *A&A*, 505, 63
- Guzman, R., Gallego, J., Koo, D. C., Phillips, A. C., Lowenthal, J. D., Faber, S. M., Illingworth, G. D., & Vogt, N. P. 1997, *ApJ*, 489, 559
- Guzmán, R., Östlin, G., Kunth, D., Bershad, M. A., Koo, D. C., & Pahre, M. A. 2003, *ApJ*, 586, L45
- Hägele, G. F., Pérez-Montero, E., Díaz, Á. I., Terlevich, E., & Terlevich, R. 2006, *MNRAS*, 372, 293
- Hägele, G. F., Díaz, Á. I., Terlevich, E., Terlevich, R., Pérez-Montero, E., & Cardaci, M. V. 2008, *MNRAS*, 383, 209
- Heckman, T. M., et al. 2005, *ApJ*, 619, L35
- Henry, R. B. C., Nava, A., & Prochaska, J. X. 2006, *ApJ*, 647, 984
- Holtzman et al. 1995, *PASP*, 107, 1065
- Hoopes, C. G., et al. 2007, *ApJS*, 173, 441
- Hoyos, C., Koo, D. C., Phillips, A. C., Willmer, C. N. A., & Guhathakurta, P. 2005, *ApJ*, 635, L21
- Hu, E. M., Cowie, L. L., & McMahon, R. G. 1998, *ApJ*, 502, L99
- Izotov et al. 1997, *ApJ*, 476, 698
- Izotov, Y. I., & Thuan, T. X. 1999, *ApJ*, 511, 639
- Izotov, Y. I., Stasińska, G., Meynet, G., Guseva, N. G., & Thuan, T. X. 2006, *A&A*, 448, 955
- Izotov, Y. I., Guseva, N. G., & Thuan, T. X. 2011, *ApJ*, 728, 161
- James, B. L., Tsamis, Y. G., Barlow, M. J., Westmoquette, M. S., Walsh, J. R., Cuisinier, F., & Exter, K. M. 2009, *MNRAS*, 398, 2
- Kakazu, Y., Cowie, L. L., & Hu, E. M. 2007, *ApJ*, 668, 853
- Kehrig, C., Vílchez, J. M., Telles, E., Cuisinier, F., & Pérez-Montero, E. 2006, *A&A*, 457, 477
- Kehrig, C., Vílchez, J. M., Sánchez, S. F., et al. 2008, *A&A*, 477, 813
- Kobulnicky, H. A., & Skillman, E. D. 1996, *ApJ*, 471, 211
- Kobulnicky, H. A., & Skillman, E. D. 1997, *ApJ*, 489, 636
- Koo, D. C., Bershad, M. A., Wirth, G. D., Stanford, S. A., & Majewski, S. R. 1994, *ApJ*, 427, L9
- Köppen, J., & Edmunds, M. G. 1999, *MNRAS*, 306, 317
- Köppen, J., & Hensler, G. 2005, *A&A*, 434, 531
- Krueger, H., Fritze-v. Alvensleben, U., & Loose, H.-H. 1995, *A&A*, 303, 41
- Kunth, D., & Sargent, W. L. W. 1981, *A&A*, 101, L5
- Lee, J. C., Salzer, J. J., & Melbourne, J. 2004, *ApJ*, 616, 752
- Leitherer, C., et al. 1999, *ApJS*, 123, 3

- Lilly, S. J., Le Fevre, O., Hammer, F., & Cramp-ton, D. 1996, *ApJ*, 460, L1
- Lintott, C. J., et al. 2008, *MNRAS*, 389, 1179
- Lintott, C., et al. 2011, *MNRAS*, 410, 166
- Lodders, K. 2003, *ApJ*, 591, 1220
- López-Sánchez, Á. R., Esteban, C., García-Rojas, J., Peimbert, M., & Rodríguez, M. 2007, *ApJ*, 656, 168
- López-Sánchez, Á. R., & Esteban, C. 2010, *A&A*, 516, A104
- López-Sánchez, Á. R., Mesa-Delgado, A., López-Martín, L., & Esteban, C. 2011, *MNRAS*, 411, 2076
- Lowenthal, J. D., et al. 1997, *ApJ*, 481, 673
- Luridiana, V., Peimbert, A., Peimbert, M., & Cerviño, M. 2003, *ApJ*, 592, 846
- Mallery, R. P., et al. 2007, *ApJS*, 173, 482
- Martín-Manjón, M. L., García-Vargas, M. L., Mollá, M., & Díaz, A. I. 2010, *MNRAS*, 403, 2012
- Masegosa, J., Moles, M., & del Olmo, A. 1991, *A&A*, 244, 273
- Masegosa, J., Moles, M., & Campos-Aguilar, A. 1994, *ApJ*, 420, 576
- Mateus, A., Sodré, L., Cid Fernandes, R., Stasińska, G., Schoenell, W., & Gomes, J. M. 2006, *MNRAS*, 370, 721
- Mollá, M., Vílchez, J. M., Gavilán, M., & Díaz, A. I. 2006, *MNRAS*, 372, 1069
- Mollá, M., García-Vargas, M. L., & Bressan, A. 2009, *MNRAS*, 398, 451
- Monreal-Ibero, A., Vílchez, J. M., Walsh, J. R., & Muñoz-Tuñón, C. 2010, *A&A*, 517, A27
- Nava, A., Casebeer, D., Henry, R. B. C., & Jevremovic, D. 2006, *ApJ*, 645, 1076
- Noeske, K. G., Papaderos, P., Cairós, L. M., & Fricke, K. J. 2003, *A&A*, 410, 481
- Noeske, K. G., Koo, D. C., Phillips, A. C., Willmer, C. N. A., Melbourne, J., Gil de Paz, A., & Papaderos, P. 2006, *ApJ*, 640, L143
- Noeske, K. G., et al. 2007, *ApJ*, 660, L43
- Olive, K. A., & Skillman, E. D. 2004, *ApJ*, 617, 29
- Östlin, G., Amram, P., Bergvall, N., et al. 2001, *A&A*, 374, 800
- Overzier, R. A., et al. 2008, *ApJ*, 677, 37
- Overzier, R. A., et al. 2009, *ApJ*, 706, 203
- Overzier, R. A., Heckman, T. M., Schiminovich, D., Basu-Zych, A., Gonçalves, T., Martin, D. C., & Rich, R. M. 2010, *ApJ*, 710, 979
- Overzier, R. A., et al. 2011, *ApJ*, 726, L7
- Pagel, B. E. J., Terlevich, R. J., & Melnick, J. 1986, *PASP*, 98, 1005
- Pagel, B. E. J., Simonson, E. A., Terlevich, R. J., & Edmunds, M. G. 1992, *MNRAS*, 255, 325
- Papaderos, P., Loose, H.-H., Fricke, K. J., & Thuan, T. X. 1996, *A&A*, 314, 59
- Papaderos, P., Izotov, Y. I., Fricke, K. J., Thuan, T. X., & Guseva, N. G. 1998, *A&A*, 338, 43
- Papaderos, P., Izotov, Y. I., Thuan, T. X., Noeske, K. G., Fricke, K. J., Guseva, N. G., Green, R. F. 2002, *A&A*, 393, 461
- Papaderos, P., Guseva, N. G., Izotov, Y. I., & Fricke, K. J. 2008, *A&A*, 491, 113
- Pilyugin, L. S. 1992, *A&A*, 260, 58
- Pérez-Montero, E. & Díaz, A. I. 2003, *MNRAS*, 346, 105.
- Pérez-Montero, E., Díaz, A. I., Vílchez, J. M., & Kehrig, C. 2006, *A&A*, 449, 193
- Pérez-Montero E., Hägele G. F., Contini T., Díaz Á. I., 2007, *MNRAS*, 381, 125
- Pérez-Montero, E., Contini, T., Lamareille, F., et al. 2009, *A&A*, 495, 73
- Pérez-Montero, E., & Contini, T. 2009, *MNRAS*, 398, 949

- Pérez-Montero, E., García-Benito, R., Hägele, G. F., & Díaz, Á. I. 2010, *MNRAS*, 404, 2037
- Pérez-Montero, E., Vílchez, J. M., Cedrés, B., et al. 2011, *A&A*, 532, A141
- Pettini, M., Shapley, A. E., Steidel, C. C., Cuby, J.-G., Dickinson, M., Moorwood, A. F. M., Adelberger, K. L., & Giavalisco, M. 2001, *ApJ*, 554, 981
- Phillips, A. C., Guzman, R., Gallego, J., Koo, D. C., Lowenthal, J. D., Vogt, N. P., Faber, S. M., & Illingworth, G. D. 1997, *ApJ*, 489, 543
- Pilyugin, L. S. 1993, *A&A*, 277, 42
- Pilyugin, L. S., Thuan, T. X., & Vílchez, J. M. 2003, *A&A*, 397, 487
- Pilyugin, L. S., Vilchez, J. M., Mattsson, L., & Thuan, T. X. 2012, arXiv:1201.1554
- Primack, J. R., Somerville, R. S., Faber, S. M., & Wechsler, R. H. 1998, *Phys. Rep.*, 307, 15
- Renzini, A., & Voli, M. 1981, *A&A*, 94, 175
- Reverte, D., Vílchez, J. M., Hernández-Fernández, J. D., & Iglesias-Páramo, J. 2007, *AJ*, 133, 705
- Rodríguez, M., & Rubin, R. H. 2004, *Recycling Intergalactic and Interstellar Matter*, 217, 188
- Salim, S., et al. 2007, *ApJS*, 173, 267
- Salzer, J. J., Williams, A. L., & Gronwall, C. 2009, *ApJ*, 695, L67
- Sargent, W. L. W., & Searle, L. 1970, *ApJ*, 162, L155
- Schaerer, D., & Vacca, W. D. 1998, *ApJ*, 497, 618
- Schaerer, D., Contini, T., & Pindao, M. 1999, *A&AS*, 136, 35
- Schlegel, D. J., Finkbeiner, D. P., & Davis, M. 1998, *ApJ*, 500, 525
- Silich, S., Tenorio-Tagle, G., Muñoz-Tuñón, C., Hueyotl-Zahuantitla, F., Wünsch, R., & Palouš, J., *ApJ*, 711, 25
- Steidel, C. C., Adelberger, K. L., Giavalisco, M., Dickinson, M., & Pettini, M. 1999, *ApJ*, 519, 1
- Storey, P. J., & Hummer, D. G. 1995, *MNRAS*, 272, 41
- Tenorio-Tagle, G., Muñoz-Tuñón, C., Pérez, E., Silich, S., & Telles, E. 2006, *ApJ*, 643, 186
- Telles, E., Melnick, J., & Terlevich, R. 1997, *MNRAS*, 288, 78
- Terlevich, R., Melnick, J., Masegosa, J., Moles, M., & Copetti, M. V. F. 1991, *A&AS*, 91, 285
- Vacca, W. D., & Conti, P. S. 1992, *ApJ*, 401, 543
- Vaduvescu, O., Richer, M. G., & McCall, M. L. 2006, *AJ*, 131, 1318
- van der Wel, A., Straughn, A. N., Rix, H.-W., et al. 2011, *ApJ*, 742, 111
- van Zee, L., Salzer, J. J., & Haynes, M. P. 1998, *ApJ*, 497, L1
- van Zee, L., & Haynes, M. P. 2006, *ApJ*, 636, 214
- Vila Costas, M. B., & Edmunds, M. G. 1993, *MNRAS*, 265, 199
- Werk, J. K., Jangren, A., & Salzer, J. J. 2004, *ApJ*, 617, 1004

TABLE 1
MAIN PROPERTIES OF THE GALAXIES FROM THE LITERATURE

ID SDSS	RA $J2000$ deg	DEC $J2000$ deg	z	m_g	M_g	$E(B - V)$	r_e kpc	L_{FUV} L_\odot	$\text{SFR}_{H\alpha+24}$ $M_\odot \text{ yr}^{-1}$	M_\star M_\odot	$12+\log(\text{O}/\text{H})$ dex
J004054	10.22635	15.56938	0.283	20.86	-19.68	0.065	0.95	10.43	13.6	9.2 ^a	8.03 ^a
J113303	173.26578	65.22815	0.241	20.02	-20.16	0.011	0.77	10.72	7.7	9.30 ^b	7.97 ^b , 8.00 ^c
J232539	351.41345	0.75200	0.277	20.17	-20.32	0.037	0.81	10.52	12.8	9.41 ^b	8.29 ^b , 8.18 ^c

NOTE.—Redshifts (z) were taken from SDSS DR7. $E(B - V)$ values are from Schlegel et al. (1998). Magnitudes are not corrected from galactic and internal extinction. Absolute magnitudes were calculated as $M_g = m_g + 5 - 5 \log(D_L) + 2.5 \log(1 + z)$, where D_L is the luminosity distance and m_g is the Sloan g' -band apparent magnitude (m_{petro}). Half-light radius (r_e), obtained from WFPC2/HST optical broad-band imaging, and dust-corrected total SFRs are from Overzier et al. (2009). Logarithm of the FUV luminosity (L_{FUV}) was taken from Hoopes et al. (2007).

^aFrom Overzier et al. (2009)

^bFrom Izotov et al. (2011)

^cValues obtained and used by Amorín et al. (2010). they were derived using the direct method in the case of GP113303, and the N2 calibration for GP232539.

TABLE 2
OSIRIS-GTC LOG OF OBSERVATIONS

ID	CCD Chip	Slit ^a /Filter	T_{exp}	Airmass	Seeing	Date	Comment
GP004054	2	Sloan z'	2250s	1.10-1.25	<1.0	2010-07-08	clear/dark
...	2	R1000B	3870s	1.1-1.2	1.2	2010-07-11	spectroscopic-dust/dark
...	2	R1000R	3870s	1.13-1.26	1.0	2010-07-17	clear/dark
...	2	R1000R	3870s	1.12-1.25	1.0-1.1	2010-08-02	clear-dust/dark
GP113303	2	Sloan z'	2250s	1.45-1.60	1.0	2010-05-21	photometric/gray
...	1	R1000B	3870s	1.35-1.45	<1.2	2010-06-03	photometric/gray
...	1	R1000R	3870s	1.80-2.00	1.1-1.4	2010-07-09	clouds-dust/dark
GP232539	2	Sloan z'	2250s	1.3-1.5	<1.2	2010-07-07	clear-dust/dark
...	1	R1000B	2580s	1.14	1.0	2010-07-09	cloudy-dust/dark
...	2	R1000B	1290s	1.43	1.4	2010-07-12	cloudy-dust/dark
...	1	R1000R	3870s	1.13-1.18	1.4	2010-07-10	spectroscopic-dust/dark

^aIn all cases the spectroscopic observations were done with a 0.8 arcsec wide slit located in the parallactic angle.

TABLE 3
MEASURED AND EXTINCTION-CORRECTED LINE FLUXES AND LINE IDENTIFICATIONS

λ , Line id.	$f(\lambda)$	GP004054		GP113303		GP232539	
		F(λ)	I(λ)	F(λ)	I(λ)	F(λ)	I(λ)
3188 HeI	0.47	20 \pm 2	28 \pm 4	—	—	32 \pm 14	51 \pm 22
3499 HeI	0.37	11 \pm 2	14 \pm 2	—	—	—	—
3531 HeI	0.36	—	—	25 \pm 2	30 \pm 5	—	—
3697 H17	0.33	9 \pm 1	12 \pm 1	—	—	—	—
3704 H16+HeI	0.33	11 \pm 2	14 \pm 3	15 \pm 3	17 \pm 4	8 \pm 1	11 \pm 2
3712 H15	0.33	12 \pm 1	15 \pm 1	—	—	10 \pm 5	13 \pm 7
3727 [OII]	0.32	1314 \pm 4	1680 \pm 87	1443 \pm 14	1675 \pm 212	1815 \pm 8	2479 \pm 111
3750 H12	0.32	23 \pm 2	30 \pm 3	—	—	9 \pm 2	12 \pm 3
3770 H11	0.31	31 \pm 4	39 \pm 5	21 \pm 5	24 \pm 6	14 \pm 3	19 \pm 4
3798 H10	0.31	34 \pm 1	43 \pm 3	29 \pm 1	33 \pm 4	32 \pm 6	43 \pm 8
3820 HeI	0.30	18 \pm 2	23 \pm 3	—	—	8 \pm 1	11 \pm 2
3835 H9	0.30	56 \pm 2	71 \pm 4	52 \pm 3	60 \pm 8	29 \pm 3	39 \pm 5
3868 [NeIII]	0.29	389 \pm 10	486 \pm 26	470 \pm 5	538 \pm 62	308 \pm 12	409 \pm 23
3889 HeI+H8	0.29	150 \pm 4	186 \pm 10	154 \pm 4	176 \pm 20	143 \pm 5	189 \pm 10
3916 NII	0.28	—	—	68 \pm 11	78 \pm 15	—	—
3968 [NeIII]+H7	0.27	287 \pm 4	351 \pm 16	252 \pm 6	285 \pm 31	182 \pm 6	235 \pm 12
4026 [NII]+HeI	0.25	23 \pm 4	28 \pm 5	—	—	10 \pm 2	13 \pm 2
4102 H δ	0.23	247 \pm 3	294 \pm 11	263 \pm 10	293 \pm 29	218 \pm 6	272 \pm 11
4243 [FeII]	0.19	—	—	25 \pm 3	27 \pm 4	—	—
4340 H γ	0.16	463 \pm 4	522 \pm 14	418 \pm 4	449 \pm 28	437 \pm 5	508 \pm 13
4363 [OIII]	0.15	79 \pm 3	88 \pm 4	84 \pm 3	90 \pm 6	64 \pm 11	74 \pm 12
4471 HeI	0.12	40 \pm 1	44 \pm 1	37 \pm 6	39 \pm 7	33 \pm 3	37 \pm 4
4571 MgI	0.08	7 \pm 1	7 \pm 1	—	—	—	—
4658 [FeIII]	0.06	18 \pm 2	19 \pm 2	18 \pm 4	18 \pm 4	18 \pm 2	19 \pm 2
4686 HeII	0.05	14 \pm 2	14 \pm 2	—	—	—	—
4702 [FeIII]	0.05	3 \pm 0	3 \pm 1	—	—	—	—
4713 [ArIV]+HeI	0.04	12 \pm 1	13 \pm 1	9 \pm 2	9 \pm 2	5 \pm 1	5 \pm 1
4740 [ArIV]	0.03	9 \pm 1	9 \pm 1	—	—	—	—
4815 [FeII]	0.01	6 \pm 1	6 \pm 1	16 \pm 5	16 \pm 5	—	—
4861 H β	0.00	1000 \pm 3	1000 \pm 3	1000 \pm 6	1000 \pm 6	1000 \pm 5	1000 \pm 5
4881 [FeIII]	0.00	—	—	19 \pm 2	19 \pm 2	7 \pm 1	7 \pm 1
4921 HeI	-0.02	13 \pm 3	13 \pm 3	—	—	4 \pm 2	4 \pm 2
4959 [OIII]	-0.03	2017 \pm 8	1978 \pm 11	1918 \pm 11	1895 \pm 22	1404 \pm 8	1369 \pm 9
4986 [FeIII]	-0.03	14 \pm 2	13 \pm 2	14 \pm 6	13 \pm 6	12 \pm 1	12 \pm 1
5007 [OIII]	-0.04	6080 \pm 13	5907 \pm 38	5499 \pm 27	5404 \pm 84	4209 \pm 24	4058 \pm 31
5199 [NI]	-0.08	12 \pm 2	11 \pm 1	—	—	30 \pm 3	28 \pm 3
5876 HeI	-0.20	131 \pm 3	112 \pm 5	128 \pm 2	117 \pm 9	141 \pm 5	116 \pm 6
6046 [OI]	-0.23	31 \pm 18	26 \pm 16	—	—	—	—
6300 [OI]	-0.26	55 \pm 2	45 \pm 3	82 \pm 9	72 \pm 11	87 \pm 8	68 \pm 7
6312 [SIII]	-0.26	26 \pm 6	21 \pm 5	43 \pm 6	38 \pm 7	26 \pm 8	20 \pm 6
6364 [OI]	-0.27	15 \pm 1	12 \pm 1	—	—	28 \pm 7	22 \pm 5
6548 [NII]	-0.30	64 \pm 10	51 \pm 8	21 \pm 10	18 \pm 9	38 \pm 11	28 \pm 9
6563 H α	-0.30	3588 \pm 12	2861 \pm 138	2952 \pm 33	2573 \pm 301	3878 \pm 49	2907 \pm 125
6584 [NII]	-0.30	148 \pm 6	117 \pm 7	172 \pm 6	150 \pm 20	332 \pm 4	248 \pm 11
6678 HeI	-0.31	41 \pm 1	32 \pm 2	141 \pm 10	122 \pm 17	41 \pm 2	30 \pm 2
6717 [SII]	-0.32	193 \pm 4	152 \pm 8	157 \pm 10	136 \pm 19	330 \pm 5	243 \pm 11
6731 [SII]	-0.32	149 \pm 3	117 \pm 6	165 \pm 21	142 \pm 25	253 \pm 8	185 \pm 10
7065 HeI	-0.36	43 \pm 8	33 \pm 6	—	—	37 \pm 13	26 \pm 9
7083 [ArI]	-0.37	8 \pm 1	6 \pm 1	—	—	28 \pm 2	20 \pm 2
7136 [ArIII]	-0.37	91 \pm 6	69 \pm 6	—	—	84 \pm 4	59 \pm 4
7388 [Fe II]	-0.41	—	—	—	—	17 \pm 1	11 \pm 1
7499 HeI	-0.42	67 \pm 2	48 \pm 4	—	—	13 \pm 2	9 \pm 1
c(H β)		0.33 \pm 0.07		0.20 \pm 0.17		0.42 \pm 0.05	
-W(H β) (Å)		156		74		60	
F(H β)		18.7		15.4		20.2	

NOTE.—Wavelengths in Col. 1 (λ) are rest-frame. Measured [F(λ)] and extinction-corrected [I(λ)] emission-line fluxes are relative to F(H β) = I(H β) = 1000 with their corresponding errors. We also give for each galaxy the

corresponding constants of reddening $[c(\text{H}\beta)]$, the $\text{H}\beta$ emission-line extinction-corrected total flux in units of 10^{-14} $\text{erg s}^{-1} \text{ cm}^2 \text{ \AA}^{-1}$, and the $\text{H}\beta$ equivalent width.

TABLE 4
DERIVED PHYSICAL CONDITIONS AND CHEMICAL ABUNDANCES

Object	GP004054	GP113303	GP232539
$n_e([\text{SII}]) \text{ (cm}^{-3}\text{)}$	< 260	< 680	< 210
$t_e([\text{OIII}]) \text{ (10}^4 \text{ K)}$	1.34 ± 0.02	1.39 ± 0.04	1.46 ± 0.11
$t_e([\text{OII}])^a \text{ (10}^4 \text{ K)}$	1.52 ± 0.02	1.60 ± 0.02	1.60 ± 0.07
$t_e([\text{NII}]) \text{ (10}^4 \text{ K)}$	1.26 ± 0.01	1.29 ± 0.02	1.32 ± 0.04
$t_e([\text{SIII}])^b \text{ (10}^4 \text{ K)}$	1.27 ± 0.15	1.34 ± 0.16	1.42 ± 0.20
$y^+ \text{ (4471)}$	0.090 ± 0.002	0.078 ± 0.014	0.077 ± 0.009
$y^+ \text{ (5876)}$	0.088 ± 0.004	0.086 ± 0.007	0.090 ± 0.004
$y^+ \text{ (6678)}$	0.088 ± 0.006	–	0.084 ± 0.007
$y^+ \text{ (7065)}^c$	0.110 ± 0.020	–	0.082 ± 0.028
$y^{2+} \text{ (4686)}$	0.0012 ± 0.0001	–	–
y	0.089 ± 0.002	0.089 ± 0.004	0.087 ± 0.004
$12+\log(\text{O}^+/\text{H}^+)$	7.19 ± 0.04	7.15 ± 0.07	7.30 ± 0.10
$12+\log(\text{O}^{+2}/\text{H}^+)$	7.91 ± 0.02	7.82 ± 0.03	7.65 ± 0.05
$12+\log(\text{O}/\text{H})$	7.98 ± 0.06	7.91 ± 0.10	7.81 ± 0.14
$12+\log(\text{N}^+/\text{H}^+)$	6.13 ± 0.01	6.11 ± 0.02	6.31 ± 0.04
$\text{ICF}(\text{N}^+)$	6.18 ± 0.18	5.73 ± 0.23	3.21 ± 0.59
$12+\log(\text{N}/\text{H})$	6.92 ± 0.02	6.87 ± 0.03	6.82 ± 0.08
$\log(\text{N}/\text{O})$	-1.06 ± 0.04	-1.04 ± 0.08	-0.99 ± 0.11
$12+\log(\text{Ne}^{+2}/\text{H}^+)$	7.27 ± 0.03	7.26 ± 0.06	7.08 ± 0.08
$\text{ICF}(\text{Ne}^{+2})$	1.08 ± 0.04	1.08 ± 0.06	1.11 ± 0.11
$12+\log(\text{Ne}/\text{H})$	7.30 ± 0.03	7.30 ± 0.06	7.13 ± 0.09
$\log(\text{Ne}/\text{O})$	-0.68 ± 0.07	-0.61 ± 0.12	-0.68 ± 0.17
$12+\log(\text{Ar}^{+2}/\text{H}^+)$	5.54 ± 0.04	–	5.40 ± 0.04
$12+\log(\text{Ar}^{+3}/\text{H}^+)$	4.57 ± 0.05	–	–
$\text{ICF}(\text{Ar})$	1.04 ± 0.04	–	3.00 ± 1.44
$12+\log(\text{Ar}/\text{H})$	5.60 ± 0.10	–	5.88 ± 0.22
$\log(\text{Ar}/\text{O})$	-2.31 ± 0.10	–	-1.77 ± 0.23
$12+\log(\text{S}^+/\text{H}^+)$	4.74 ± 0.15	4.76 ± 0.25	4.94 ± 0.14
$12+\log(\text{S}^{+2}/\text{H}^+)$	6.32 ± 0.25	6.49 ± 0.24	6.13 ± 0.27
$\text{ICF}(\text{S})$	1.51 ± 0.40	1.55 ± 0.55	1.27 ± 0.27
$12+\log(\text{S}/\text{H})$	6.51 ± 0.35	6.69 ± 0.62	6.26 ± 0.36
$\log(\text{S}/\text{O})$	-1.48 ± 0.36	-1.22 ± 0.43	-1.55 ± 0.39
$12+\log(\text{Fe}^{2+})$	5.69 ± 0.05	5.62 ± 0.09	5.59 ± 0.08
$\text{ICF}(\text{Fe}^{2+})$	6.3 ± 4.8	7.0 ± 6.0	3.7 ± 2.7
$12+\log(\text{Fe}/\text{H})$	6.49 ± 0.25	6.39 ± 0.36	6.11 ± 0.29
$\log(\text{Fe}/\text{O})$	-1.49 ± 0.26	-1.52 ± 0.38	-1.69 ± 0.32

^aDerived from $t_e([\text{OIII}])$ using the models described in Pérez-Montero & Díaz (2003) and Pérez-Montero & Contini (2009) for $t_e([\text{OII}])$ and $t_e([\text{NII}])$, respectively

^bDerived from $t_e([\text{OIII}])$ using the empirical relation described in Hägele et al. (2006)

^cHeI 7065Å should be affected by radiative transfer effects. However, we considered here their measurements in our calculations since $y^+(7065)$ values are, within the uncertainties, in agreement with the y^+ values derived from the other helium lines.

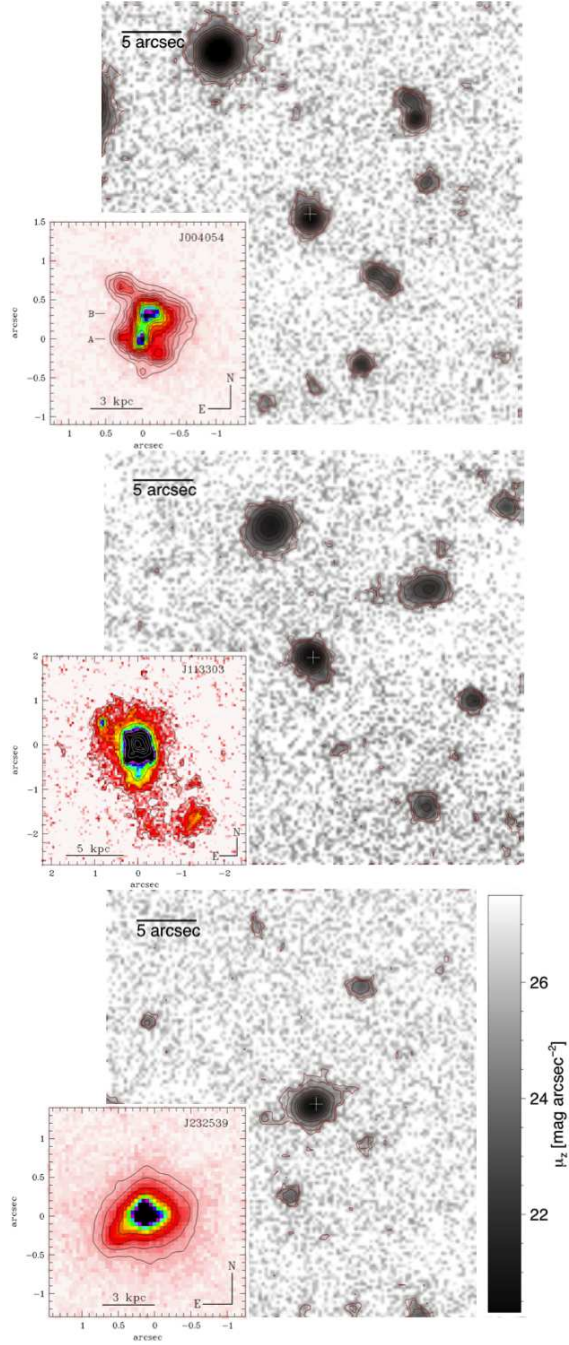


Fig. 1.— Green Pea imagery: GTC-OSIRIS z' -band images of GP004054 (upper), GP113303 (middle), and GP232539 (bottom), are shown in surface brightness grey scale, as indicated by the bar in the lower right panel. In all cases contours indicate the $\mu_z = 26$ mag arcsec $^{-2}$ level. HST WFPC2 F606W (R) images, spatially resolving the central regions of these galaxies, are showed as insets in their lower left corner. North is up and east to the left.

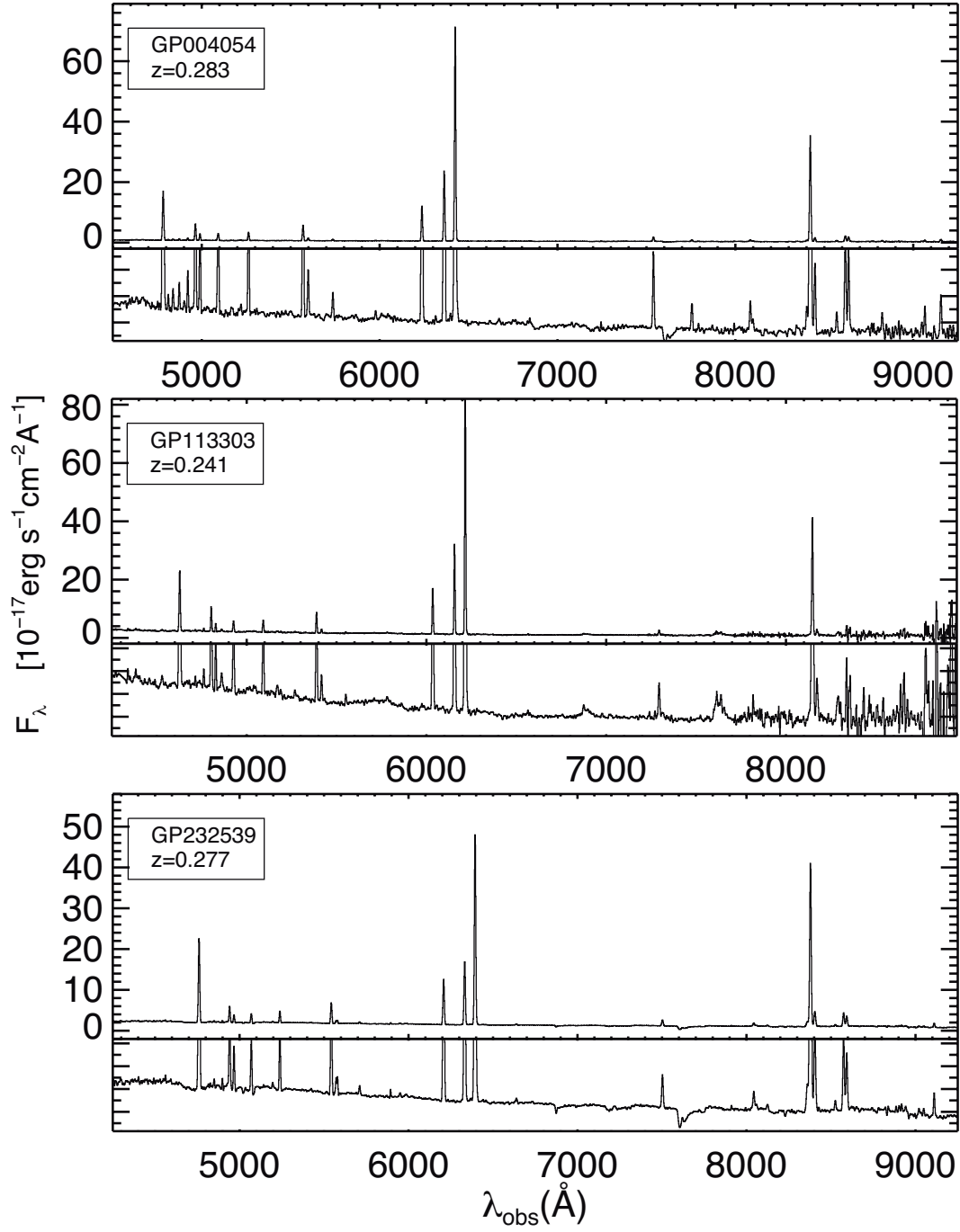


Fig. 2.— The Deep GTC-OSIRIS spectra for the three GPs under study. In order to highlight faint emission lines each spectrum is zoomed in the lower panel.

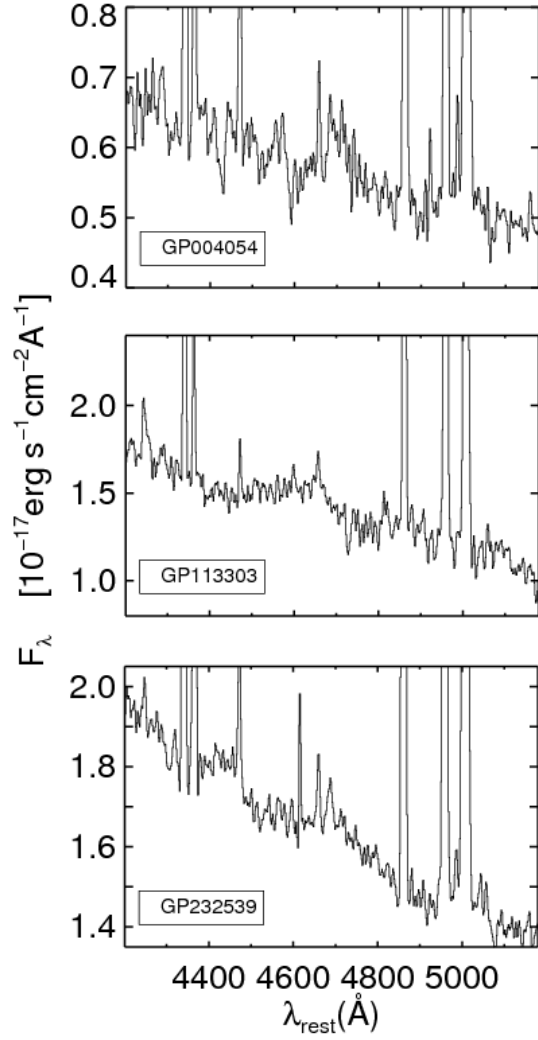


Fig. 6.— Spectra of the galaxies zoomed in the region around the Wolf-Rayet blue bump.

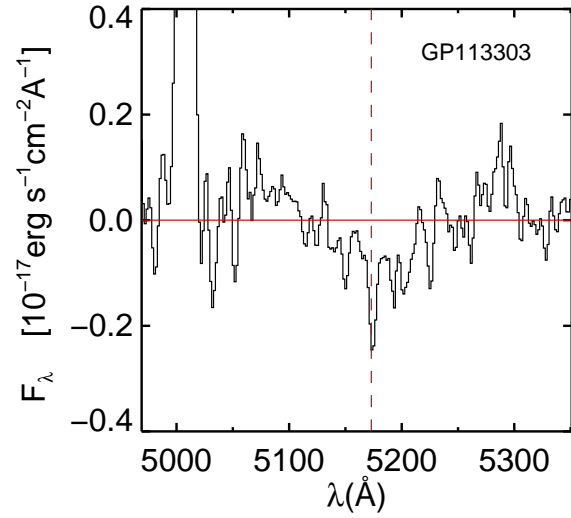


Fig. 7.— Spectrum of GP113303 zoomed in the region around the MgI absorption line after continuum subtraction. The central wavelength of the MgI $\lambda 5173$ is indicated by the vertical dashed line.

TABLE 5
MODEL RESULTS FROM STARLIGHT (RUN 1 AND RUN 2)

Galaxy	nebular continuum ^a (%)			$M_{\star, \text{young}}$ (%)	$M_{\star, \text{total}}$ (log M_{\odot})	χ^2
	[O II]	H β	H α			
RUN 1: POPSTAR MODELS						
GP004054	10	18	35	22	9.18	1.05
GP113303	3.5	6	11	4.2	9.44	0.86
GP232539	8	10.5	20	11.3	9.38	1.54
RUN 2: B&C MODELS						
GP004054	15.7	9.22	1.17
GP113303	1.9	9.68	0.95
GP232539	5.4	9.90	1.37

^aFor three different wavelength regions (around [O II], H β , and H α), columns 2, 3, and 4 give the estimated fraction nebular continuum emission derived from STARLIGHT fits to each galaxy spectrum using POPSTAR models (see text)

TABLE 6
RESULTS FROM THE TWO-COMPONENT EVOLUTIONARY SYNTHESIS MODEL (RUN 3)

Galaxy	t_{burst} (Myr)	b_{par}	$C(\text{H}\beta)$	EW(H α) (\AA)	EW(H β) (\AA)	$M_{\star, \text{young}}$ (%)	χ^2
GP004054	4	5.3	0.41	894	139	8.3	1.5
GP113303	5	4.2	0.32	445	76	6.7	2.1
GP232539	5	2.8	0.43	344	53	4.4	1.4

NOTE.—Column 2: age of the young stellar component. Column 3: burst parameter. Column 4: reddening constant predicted by the evolutionary model. Columns 5 and 6: predicted equivalent widths of H α and H β emission lines.

TABLE 7
WOLF-RAYET FEATURES DETECTED IN THE GALAXY SAMPLE

Galaxy	$I_{\text{BB}}(\lambda)$ ^a	$\log L_{\text{BB}}$ ^b	EW_{BB}	N(WR \star) ^c	N(WR \star /O \star) ^d
GP004054	34 \pm 4	40.1	4.2 \pm 0.5	806 \pm 97	0.011 \pm 0.001
GP113303	80 \pm 15	40.8	5.5 \pm 1.0	1239 \pm 228	0.029 \pm 0.005
GP232539	36 \pm 6	40.3	1.9 \pm 0.3	1145 \pm 191	0.012 \pm 0.002

^aExtinction-corrected, emission-line flux measured for the WR blue bump relative to I(H β)=1000 with their corresponding errors.

^bluminosity of the WR blue bump calculated using $I_{\text{BB}}(\lambda)$ and the distances adopted throughout the paper

^cNumber of WR stars as derived from L_{BB} and adopting a mean luminosity for a WR star $\log L_{\text{WR}\star} = 37.248$ from STARBURST99 models with stellar metallicity $Z = 0.004$ (Pérez-Montero et al. 2010)

^dWR to O star number ratio and its errors. The number of O stars were derived from $L_{\text{H}\alpha}$ and adopting a mean H α luminosity for an O star $\log L_{\text{H}\alpha, \text{O}\star} = 37.21$.

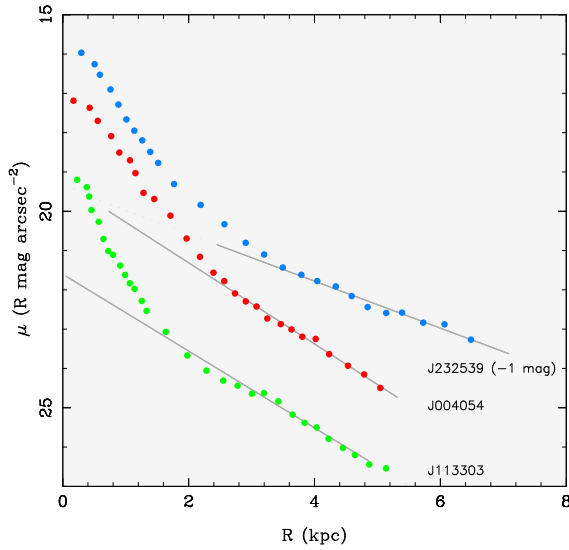


Fig. 8.— Surface brightness profiles (SBPs) of the three GPs derived from archival HST/WFPC2 R -band (F606W) images. The SBPs have been corrected for Galactic extinction and cosmological dimming but no k corrections were applied. The SBP of J232539 has been shifted by -1 mag for the sake of clarity. It can be seen that all SBPs show an extended exponential LSB envelope dominating for $\mu \gtrsim 22 - 23$ mag arcsec $^{-2}$. Linear fits to the LSB component (gray lines) yield scale lengths and central surface brightness levels of 1.5–3 kpc and 19–21.5 mag arcsec $^{-2}$, respectively.

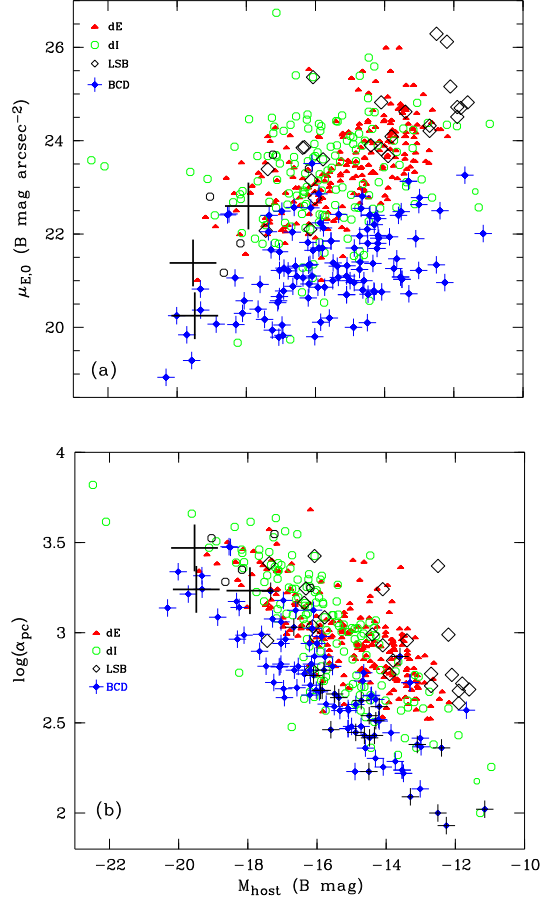


Fig. 9.— Comparison of the structural properties of the LSB component of our sample GPs (large crosses) with those of other types of low-mass galaxies compiled in Papaderos et al. (2008). Photometric quantities derived from fitting of R band profiles in Fig. 8 have been converted into B band assuming a $B - R = 1$ mag. The lower and upper panel compare, respectively, the central surface brightness and the exponential scale length vs the absolute magnitude of the LSB component of GPs with those of BCDs, dwarf irregulars (dIs), dwarf ellipticals (dEs) and LSB galaxies. It can be seen that GPs occupy roughly the same parameter space as luminous BCDs.

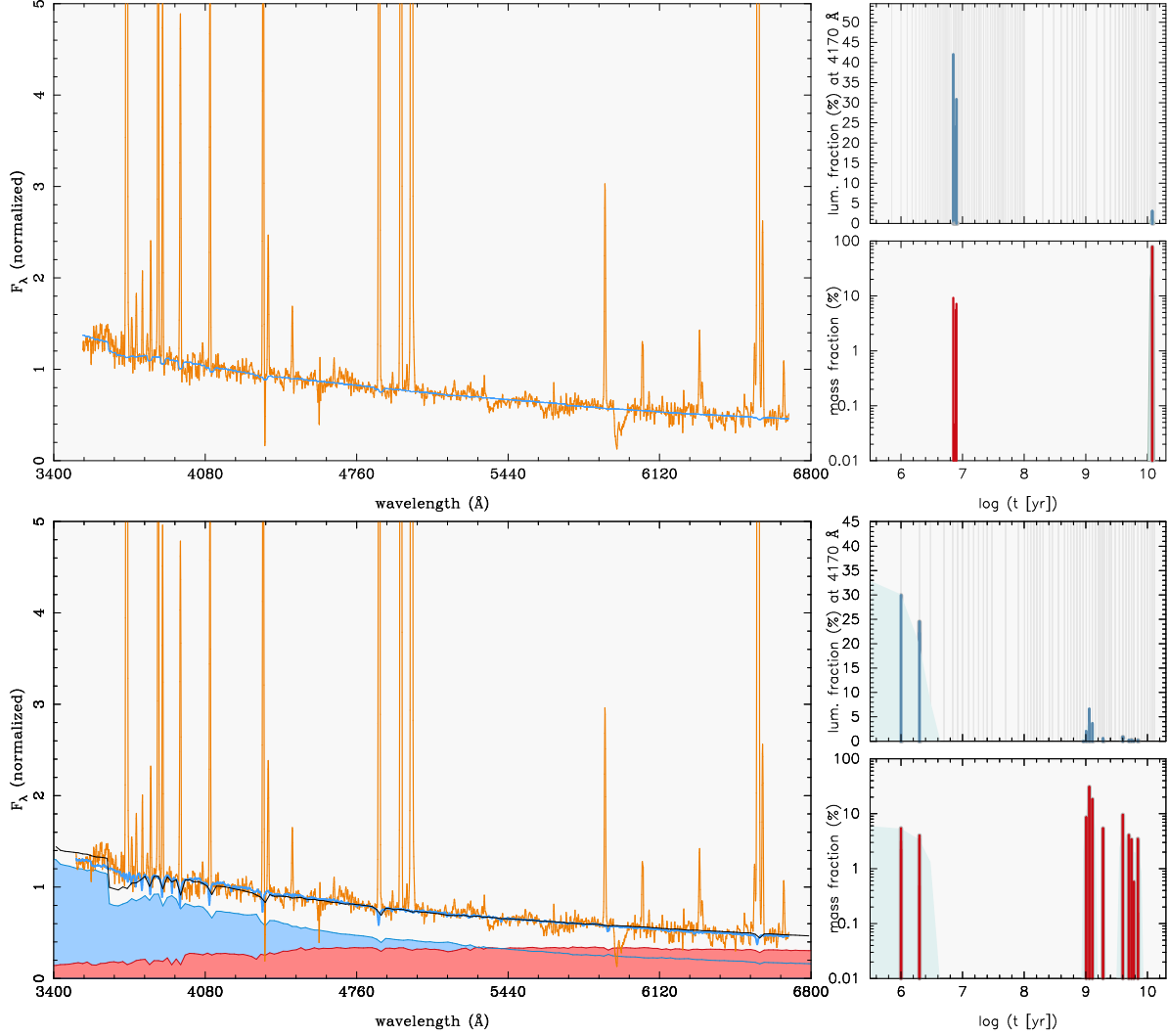


Fig. 3.— upper panel: Best-fitting synthetic SED based on POPSTAR SSPs (RUN1; blue color), overimposed on the rest-frame observed spectrum of GP004054 (orange), normalized at 4170 Å. The smaller plots on the right show the luminosity and mass contribution of individual SSPs (upper and lower panel, respectively). The age distribution of the library SSPs is illustrated by thin vertical lines in the upper panel. lower panel: Fit to the observed spectrum based on purely stellar SSPs from Bruzual & Charlot (RUN2). The color coding is as in the upper large panel. Vertical strips mark regions that have been flagged prior to spectral fitting. The best-fitting synthetic SEDs from a two-component evolutionary synthesis model (RUN3) that comprises an old and a young stellar component (red and blue shaded area, respectively), and self-consistently accounts for the observed Balmer H α and H β EWs, is overlaid in black color.

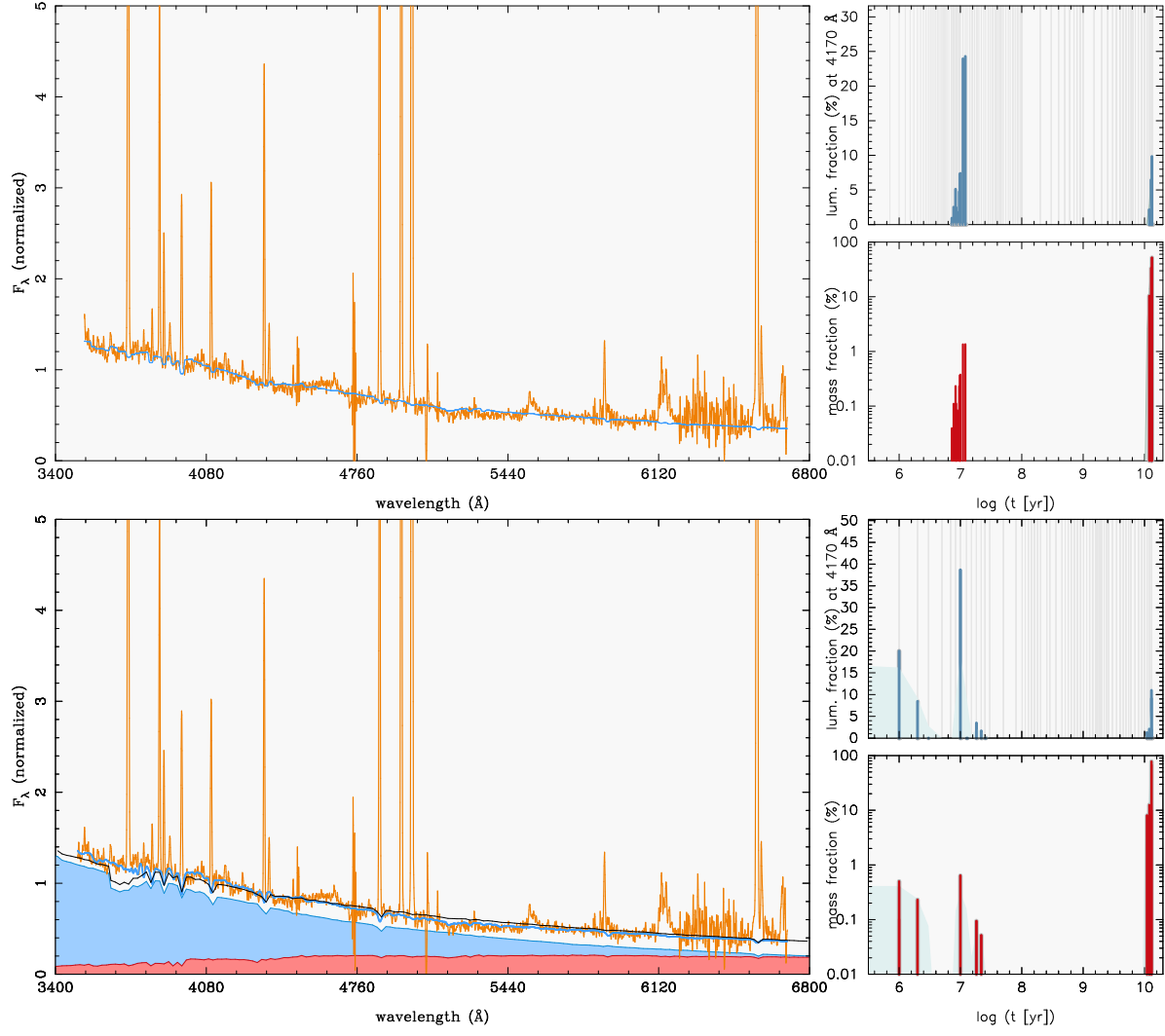


Fig. 4.— Same as Fig.3 for GP113303.

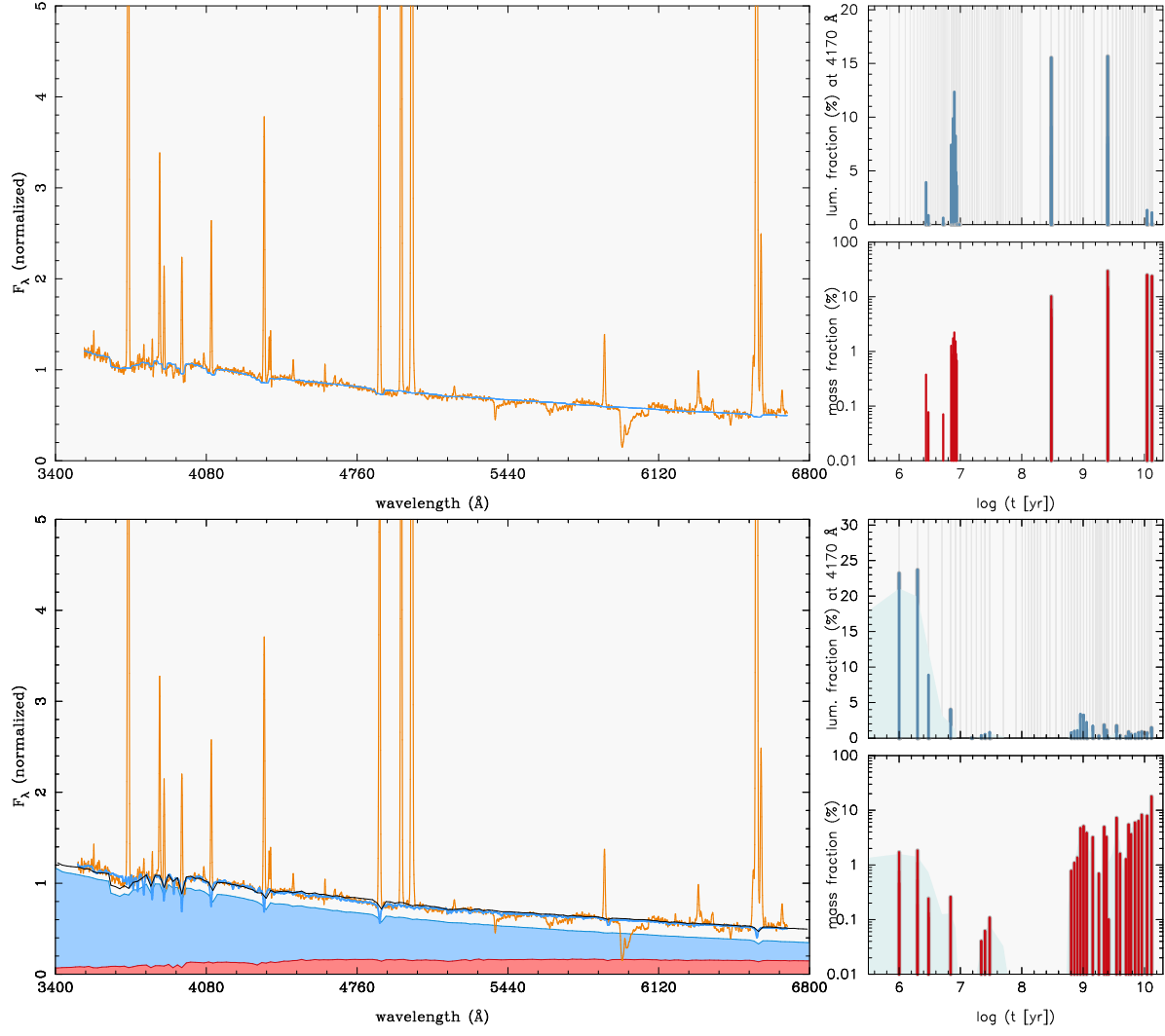


Fig. 5.— Same as Fig.3 for GP232539.